Mapping the maze: advancing atrial fibrillation models and therapies

Harlaar, N.

Citation

Harlaar, N. (2026, January 29). *Mapping the maze: advancing atrial fibrillation models and therapies*. Retrieved from https://hdl.handle.net/1887/4288215

Chapter 5

Conditional immortalization of human atrial cardiomyocytes for generating *in vitro* models of atrial fibrillation

Nat Biomed Eng. 2022;6:389-402.

Niels Harlaar, Sven O. Dekker, Juan Zhang, Rebecca R. Snabel, Marieke W. Veldkamp, Arie O. Verkerk, Carla Cofiño Fabres, Verena Schwach, Lente J.S. Lerink, Mathilde R. Rivaud, Aat A. Mulder, Willem E. Corver, Marie José T.H. Goumans, Dobromir Dobrev, Robert J.M. Klautz, Martin J. Schalij, Gert Jan C. Veenstra, Robert Passier, Thomas J. van Brakel, Daniël A. Pijnappels#, Antoine A.F. de Vries#
# Equal contribution

Abstract

Clinically relevant *in vitro* models of human disease require large numbers of human parenchymal cells like cardiomyocytes. The current lack of a scalable and robust source of well-differentiated human atrial myocytes limits the development of in vitro models of atrial fibrillation (AF). Here, we report that a lentiviral vector-based conditional cell immortalization procedure allows the production (through a quadrillion-fold cell multiplication) of large numbers of fully functional atrial myocytes. The doxycycline-controlled expression of a recombinant simian virus 40 large T gene in human foetal atrial myocytes resulted in the generation of 15 monoclonal cell lines with molecular, cellular and electrophysiological properties resembling those of primary atrial myocytes following doxycycline withdrawal. The immortalized atrial myocytes were used to create multicellular AF models. These models displayed fibrillatory activity with frequencies of 6-8 Hz, consistent with clinical AF manifestation, which could be terminated by administration of clinically approved antiarrhythmic drugs. The conditional cell immortalization method described herein may be used to generate functional lines of other human parenchymal cell types for the development of human disease models.

Introduction

Preclinical biomedical research across academia and industry strongly relies on *in vitro* models to advance pathophysiological insight and develop novel therapeutics. Human disease models based on (cultured) animal cells are becoming less popular due to 1) the growing awareness of the existence of principal differences in (patho)physiology between humans and animals and 2) the increasing public opposition to animal testing (1). This has created a large demand for difficult to obtain human parenchymal cells, including cardiomyocytes, hepatocytes and neurons. Acquisition of such terminally differentiated cell types is complicated by the fluctuating availability and inconsistent quality of source material including post-mortem samples, surgical waste, non-transplanted donor tissue and biopsies. Additionally, these cell types cannot be multiplied *in vitro* and rapidly dedifferentiate in culture, severely restricting the window of use after isolation. Also, permanent human cell lines of tumour origin or created through genetic engineering generally have not been able to recapitulate the functional properties of the primary cells from which they were derived, because in most cell types continuing proliferation inhibits differentiation (2).

Many of these drawbacks have been overcome by the establishment of human embryonic stem cell (hESC) lines (3) and, more recently, of human induced pluripotent stem cell (hiPSC) lines (4,5), in conjunction with the development of new methods to derive various differentiated cell types from them. As a result, human (pluripotent) stem cell-based 2- and 3-dimensional multicellular *in vitro* models including organoids (6) are rapidly gaining popularity for human disease modelling, target identification, drug development and therapeutic testing. A particularly attractive feature of hiPSCs is the ease with which they can be generated from individual patients allowing the development of patient-specific disease models, thereby creating unique opportunities for personalized medicine. Despite the many advantages of human (pluripotent) stem cell-based *in vitro* models, there are still several factors that limit their application: 1) Derivation of specialized cells from human (pluripotent) stem cells is often a complex and laborious process with a variable outcome; 2) Producing large numbers of specialized cells with a high degree of phenotypic uniformity from human (pluripotent) stem cells is difficult; 3) The differentiated progeny of human (pluripotent) stem cells typically has an immature phenotype and thus functionally differs from adult human cells.

In an attempt to address these limitations, we recently developed a monopartite lentiviral vector (LV)-based system for the conditional immortalization of primary mammalian cells (7,8). At the heart of this system is a recombinant simian virus 40 (SV40) large T (LT) gene, whose expression is driven by a cell type-specific promoter and can be repeatedly switched on and off by means of the tetracycline/doxycycline (dox)-controlled transcription silencer TetR-KRAB (9,10). In the present study, we employ this conditional immortalization to generate lines of human atrial myocytes (AMs) with preserved cardiomyogenic differentiation capacity. The reasons for choosing human AMs as target cells are two-fold: 1) Their highly specialized nature and specific functional properties (*i.e.* excitability and contractility), provide a stringent test for the effectiveness of our conditional cell immortalization system. 2) The rapid worldwide increase in the prevalence of atrial fibrillation (AF) (11), its high socioeconomic burden (12), the incomplete mechanistic understanding (13) along with substantial translational challenges (14) and the suboptimal treatment options (15), have created an urgent need for a robust source of human AMs to overcome the current lack of clinically relevant (*in vitro*) models of AF (16).

Transduction of human foetal AMs (hfAMs) with the TetR-KRAB-regulated LT-encoding LV resulted in the generation of 15 monoclonal cell lines designated hiAMs that rapidly proliferated in the presence of dox and differentiated into excitable and contractile cells with molecular, cellular and electrophysiological properties of AMs after dox withdrawal. These cell lines were used to establish multicellular *in vitro* AF models featuring fibrillatory activity with clinically relevant dynamics and activation frequencies, which could be terminated with traditional antiarrhythmic drugs. The development of the hiAM lines provides proof-of-concept of a versatile method to produce, in a simple and rapid manner, massive numbers of authentic human cells for comprehensive disease modelling.

Results

Generation and selection of hiAMs

To conditionally immortalize human atrial cardiomyocytes, human foetal atrial tissue (gestational age 18 weeks) was dissociated. The resulting cell suspension was transduced with LV particles containing a dox-inducible SV40 LT expression unit driven by the strong hybrid striated muscle-specific MHCK7 promoter (17), targeting the cardiomyocyte population in the atrial cell mixture

(**Figure 1a, Supplemental Figure 1**). Two to three weeks after induction of SV40 LT synthesis through addition of dox and reseeding cells at ultralow density, proliferating colonies comprising 100-200 cells appeared (**Figure 1b**). To assess whether the conditional immortalization was successful, 95 proliferating colonies were isolated, expanded and graded using predefined criteria to assess both the proliferative activity of the cells in the presence of dox and their ability to reacquire the differentiated properties of AMs following dox removal (**Figure 1c, Supplemental Figure 1**). To meet these criteria, the monoclones should display the following properties: 1) proliferate well in the presence of dox (> 15 population doublings [PDs] with a doubling time < 120 h), 2) cease proliferation following dox removal and acquire a cardiomyocyte-like phase-contrast appearance after 12 days of culture in differentiation medium, 3) stain negative for proliferation marker Ki-67 and positive for cardiac troponin T (TNNT2) at 12 days after dox withdrawal and 4) generate and conduct (typical atrial) electrical impulses following cardiomyogenic differentiation in confluent monolayers (action potential [AP] duration [APD] at 80% repolarization [APD_{80}] < 300 ms and conduction velocity [CV] > 10 cm/s) (**Figure 1d,e, Supplemental Figure 1**). Fifteen of the 95 (15.8%) monoclones, designated human immortalized AMs (hiAMs), adhered to all 4 predefined criteria indicating successful generation, through conditional immortalization, of human cardiomyocyte lines with preserved cardiomyogenic differentiation capacity.

Characterization of hiAMs during proliferation and after differentiation

Three of the 15 hiAM clones (*i.e.* hiAM clones 2.38, 2.52 and 2.90) were randomly selected for in-depth characterization (**Figure 1f**). The number of lentiviral integrations in these clones ranged from 4 to 6 (**Supplemental Table 1**). Analysis of their DNA content revealed all 3 clones to comprise predominantly cells with DNA indices between 1.7 and 1.8 (**Supplemental Figure 2, Supplemental Table 2**). The doubling time of the 3 selected hiAM clones in the presence of dox was 55 ± 5 h (**Figure 1g**). Proliferating hiAMs contained a much higher percentage of Ki-67-positive nuclei than freshly isolated hfAMs (**Figure 1h**). The low Ki-67 expression in hfAMs is consistent with the limited mitotic activity of human cardiomyocytes in the second semester of gestation (18). hiAMs could be expanded for at least 50 PDs without a noticeable reduction in proliferation rate, resulting in ≥ quadrillion-fold cell multiplication. Dox omission in the culture medium resulted in a strong (*i.e.* > 2000-fold) reduction of the SV40 LT level in hiAMs over the course of 12 days, as determined by western blotting (**Figure 1i**). At the same time, hiAMs no longer displayed any Ki-67-positive nuclei.

Figure 1 (legend on next page).

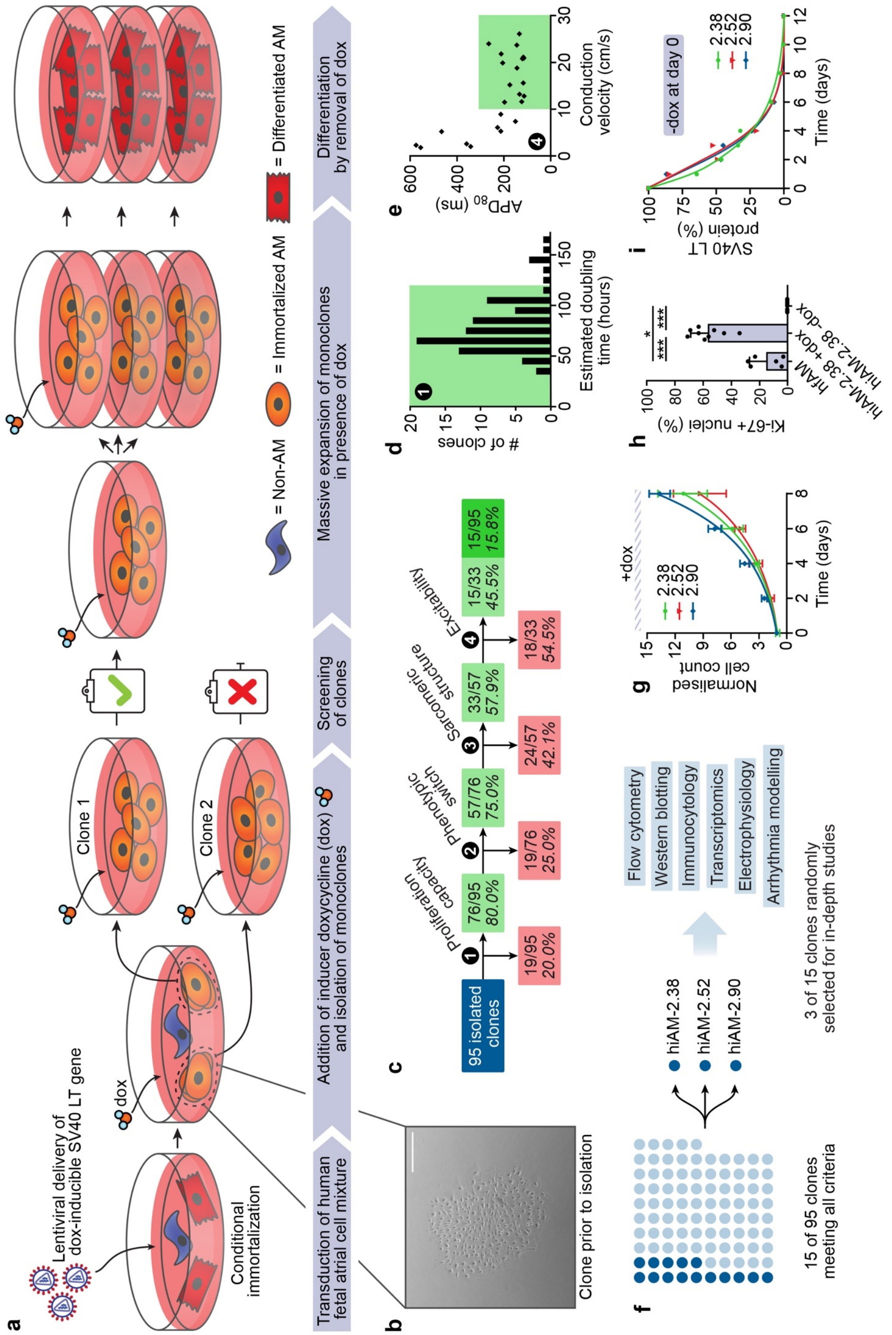

Figure 1 (previous page). Generation and selection of hiAM monoclones. **(a)** Schematic overview of the conditional immortalization of hfAMs, generation and selection of hiAM monoclones, massive hiAM expansion in the presence of dox and cardiomyogenic differentiation of hiAMs following dox removal. **(b)** Representative phase-contrast image of a hiAM monoclone prior to isolation. Scale bar, 500 µm. **(c)** Flowchart of hiAM monoclone selection based on 4 main criteria with corresponding drop-off rates (see **Supplemental Figure 1** for additional data). **(d)** Estimated doubling time of isolated hiAM monoclones based on passaging intervals. The highlighted area (doubling time ≤ 120 h) represents a pass on the first selection criterium. **(e)** Selection based on excitability of hiAM monoclones using optical voltage mapping as part of the fourth selection criterium. The highlighted area represents selected monoclones with a CV ≥ 10 cm/s and APD_{80} ≤ 300 ms. **(f)** Summary of monoclone selection. hiAM clones 2.38, 2.52 and 2.90 were selected for further characterization. **(g)** Quantification of hiAM proliferation in the presence of dox (n = 3 independent experiments per monoclone; mean shown, error bars indicate SD). **(h)** Ki-67-positive nuclei determined by immunocytochemistry in hfAM (n = 2), proliferating (+dox, n = 3) hiAM and differentiated (-dox, n = 3) hiAM cultures. Three random areas per culture were selected for quantification. n signifies independent samples/differentiations. *$P < 0.05$, ***$P < 0.001$, one-way analysis of variance with Tukey *post-hoc* analysis. Mean shown, with error bars indicating SD. **(i)** SV40 LT levels in proliferating hiAM-2.38, -2.52 and -2.90 measured by western blotting over 12 days of differentiation following removal of dox at day 0 (n = 1 per monoclone).

The 12-day transition from a proliferating to a differentiated hiAM, which is simply initiated by the removal of dox and a change from proliferation to differentiation medium, was accompanied by the reappearance of spontaneous synchronous contractions similar to those observed in freshly isolated hfAMs (**Supplemental Video 1**). Immunostaining for the sarcomeric proteins α-actinin 2 (ACTN2), TNNT2 and the atrial isoform of myosin regulatory light chain 2 (MLC2a), showed that the highly organized sarcomeres observed in hfAMs were lost following conditional immortalization and induction of proliferation, but reappeared when hiAMs were growth-arrested by dox withdrawal and allowed to redifferentiate for 12 days (**Figure 2a, Supplemental Figure 3**). Flow cytometric analysis showed that hiAM differentiation yielded highly pure cell populations, comprising on average 99.1% ACTN2-positive and 97.2% TNNT2-positive cells (**Supplemental Figure 4**). Gap junctional protein connexin 43, which was concentrated at cell-cell interfaces in hfAMs, also disappeared when proliferation was induced and again formed neatly organized cell-cell connections following hiAM differentiation (**Figure 2a**). Additionally, hiAM differentiation caused an increase in the levels of the atrium-specific gap junctional protein connexin 40 (**Supplemental Figure 3**). Detailed imaging by transmission electron microscopy revealed the presence of well-organized sarcomeres, perinuclear and intermyofibrillar mitochondria and intercalated discs in differentiated hiAMs (**Supplemental Figure 5**). Sarcomere lengths appeared to be slightly shorter in differentiated hiAMs (1.79-1.83 μm) compared to hfAMs (1.96 μm, **Supplemental Figure 3**). At all stages, hfAMs and hiAMs stained negative for the ventricular isoform of myosin regulatory light chain 2 (MLC2v), corroborating their atrial origin and specificity.

We next performed RNA-sequencing to study the transcriptome of proliferating and cardiomyogenically differentiated hiAMs (**Figure 2b**). Principal component analysis and heatmap of global gene expression data illustrated a clear separation between the transcriptomes of the proliferating (D0) and differentiated (D12) hiAM clones (**Figure 2c**). Grouped comparison revealed 6078 differentially expressed genes (DEGs), of which 2652 were downregulated and 3426 were upregulated when transitioning from proliferation to differentiation (log2-fold change > 1 and false discovery rate [FDR]-corrected $P < 0.001$, **Supplemental Data File 1**). Differential gene expression of individual clones showed a large overlap (**Figure 2d**). Downregulated genes standing out (including MKI67, AURKB, CDK1, CCNA2 and POLE) appeared to be closely involved with cell proliferation, whereas upregulated genes (such as ACTN2, MYH6, KCNJ2, CACNA1C and GJA5) were associated with a differentiated AM phenotype (**Figure 2e**). These observations were confirmed by gene ontology (GO) analysis of the up- and down-regulated genes (**Figure 2f, Supplemental Figure 6**). GO terms enriched during hiAM proliferation were mainly related to DNA replication and cell division, whereas the most enriched GO terms post-differentiation were involved in myofibrillogenesis, energy metabolism and cardiac muscle contraction. The differential expression levels of atrial and ventricular marker genes, such as MYL7/MYL2 (19669.6 vs. 0.2 transcripts per million [TPM]) and MYH6/MYH7 (1126.4 vs. 15.6 TPM), as well as the high abundance of NPPA transcripts (8494.6 TPM), further confirmed the atrial phenotype of differentiated hiAMs (**Supplemental Figure 7**). Collectively, these results demonstrate that the conditional immortalization by TetR-KRAB-regulated SV40 LT gene expression allows hfAMs to effectively switch between proliferative and differentiated states, which could not be achieved with permanent immortalization (**Supplemental Figure 8**).

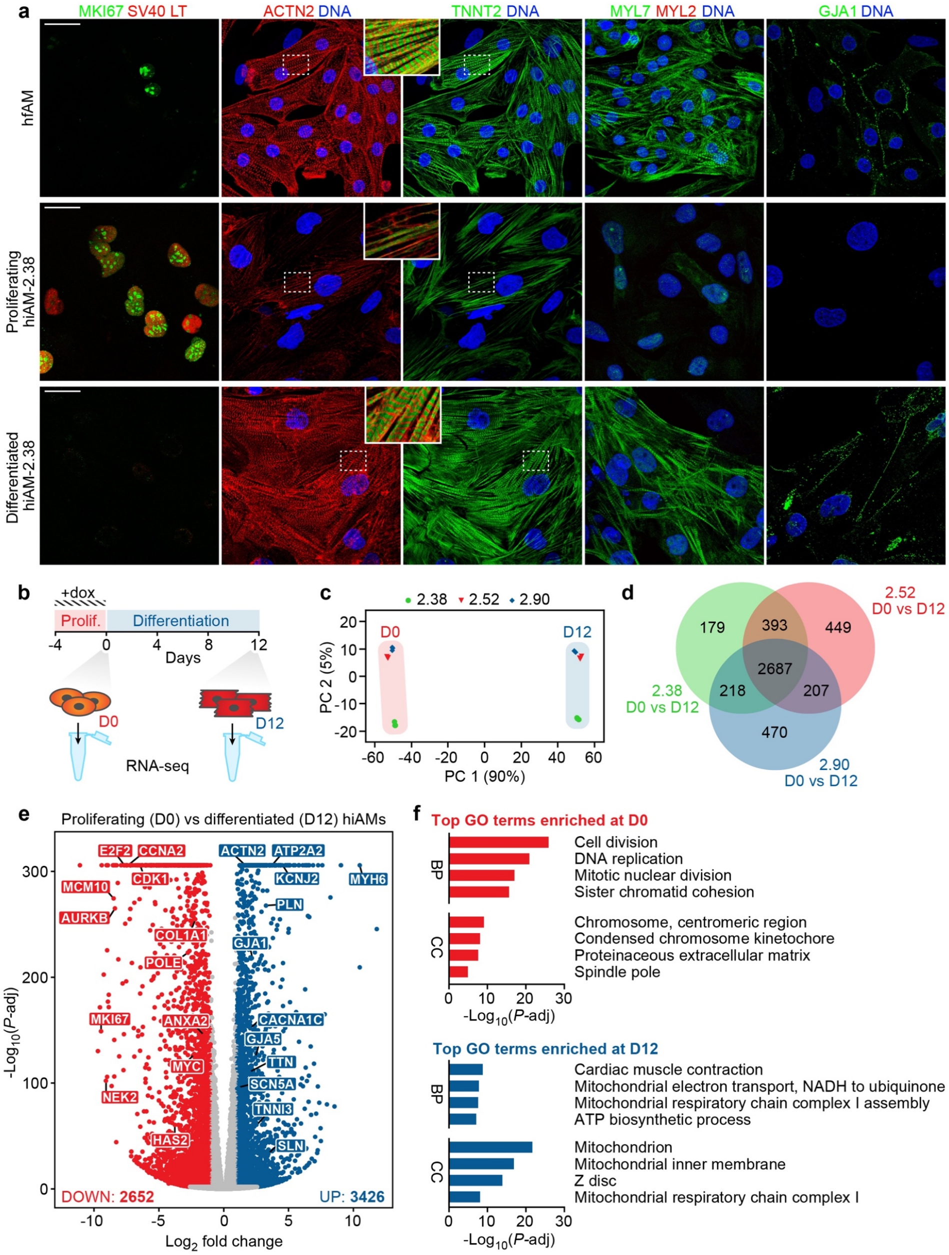

Figure 2. Characterization of the hiAM phenotype during proliferation and after 12 days of differentiation. **(a)** Immunostaining of hfAMs and of proliferating and differentiated hiAM-2.38 for Ki-67 (MKI67), SV40 LT, α-actinin 2 (ACTN2), cardiac muscle troponin T (TNNT2), the atrial and ventricular isoform of myosin regulatory light chain 2 (MYL7 and MYL2, respectively) and connexin-43 (GJA1). Scale bar, 25 μm. **(b)** Schematic representation of sample collection timeline for RNA-sequencing. **(c)** Principal

component (PC) analysis of global gene expression data (n = 3 biological replicates per time point and hiAM clone). **(d)** Venn diagram of differentially expressed genes (DEGs) between proliferating (D0) and differentiated (D12) hiAM-2.38, -2.52 and -2.90. Genes with > 1 TPM at D0 or D12, an absolute $\log_2$-fold change > 1 and an FDR-corrected $P <$ 0.001 are shown. **(e)** Volcano plot of gene expression in proliferating *vs.* differentiated hiAMs (grouped analysis of hiAM clones 2.38, 2.52 and 2.90). Selected genes of interest are labelled. Please note that due to filtering applied in the comparison of the individual clones, the number of DEGs is lower than in the grouped analysis. **(f)** Top 4 biological process (BP) and cellular component (CC) GO terms enriched in proliferating (D0) and differentiated (D12) hiAMs (see **Supplemental Figure 6** for all enriched GO terms).

Maturity of the differentiated hiAM transcriptome

Benchmarking of hiAM maturity was first performed by comparison of the global hiAM transcriptome against compendia of gene expression data from human foetal cardiac tissues (19) and human adult tissues (20). For reference purposes, also the transcriptomic maturity of hESC-derived atrial cardiomyocytes (hESC-AMs) was determined. The transcription profiles of hESC-AMs and differentiated hiAMs best correlated with those of atrial myocardium. However, the transcriptome of hESC-AMs correlated modestly better with that of foetal atrial myocardium, whereas the gene expression profile of hiAMs was somewhat closer to that of adult atrial myocardium (**Figure 3a**).

Differential gene expression analysis between hESC-AMs and hiAMs revealed 2276 DEGs upregulated in hESC-AMs and 1869 DEGs upregulated in hiAMs (**Figure 3b**). Neither of the gene sets was exclusively expressed in the heart, but overall the DEGs upregulated in hiAMs were more abundantly expressed (**Figure 3c**). Clustering analysis revealed that a subset of the upregulated DEGs had striated muscle-specific expression, which included SCN5A, CASQ2 and SLN for hiAMs, and MYL2, TTN and RYR2 for hESC-AMs (**Supplemental Figure 9, Supplemental Data File 2**). Finally, rank-based comparison of selected maturity-related gene sets in hiAMs, hESC-AMs, foetal atrial myocardium and adult atrial myocardium revealed differences in structural, electrophysiological, contractile and metabolic properties (full overview in **Supplemental Figure 10**). Overall, these data indicate that the gene expression profile of differentiated hiAMs possesses many features of the adult atrial myocardial transcriptome.

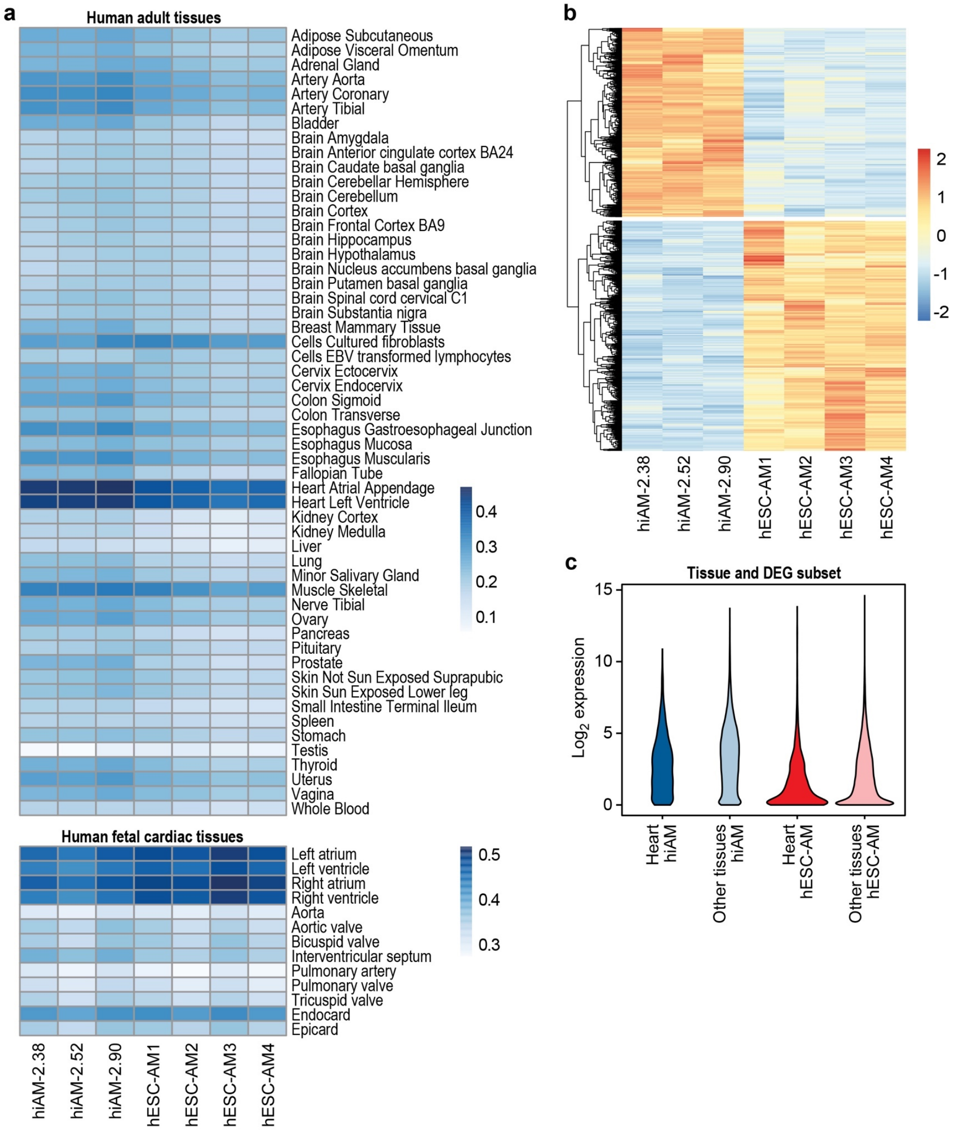

Figure 3. Characterization of differentiated hiAM and hESC-AM transcriptomes. **(a)** Global transcriptome comparison of 3 hiAM clones (hiAM-2.38, -2.52 and -2.90) and of 4 hESC-AM replicates against a compendium of human adult tissues and human foetal cardiac tissues. Scale bar indicates Spearman correlation. **(b)** Differential gene expression between hiAMs and hESC-AMs. Scale bar indicates row-scaled and centred expression values. **(c)** Expression levels of differentially expressed genes (DEGs) separated based on hiAM or hESC-AM specificity and cardiac or non-cardiac specificity.

Electrophysiological properties of differentiated hiAMs

The electrophysiological properties of cardiomyogenically differentiated hiAMs were first studied by single-cell patch-clamp analysis. Differentiated hiAM-2.38 had a resting membrane potential (RMP) similar to that of human adult AMs (haAMs) and significantly more negative than the RMP of hfAMs (**Figure 4a,b**). Additionally, the maximal AP amplitude in hiAM-2.38 was larger than in hfAMs but smaller than in haAMs, whereas the AP plateau amplitude was higher in hiAM-2.38 compared to both hfAMs and haAMs. The maximum AP upstroke velocity of hiAM-2.38 was between that of hfAMs and haAMs. APD at 20, 50 and 90% of repolarisation did not significantly differ between hfAMs, hiAM-2.38 and haAMs. AP characteristics similar to hiAM-2.38 were also observed in differentiated hiAM-2.52 and hiAM-2.90 (**Supplemental Figure 11, Supplemental Table 3**). Subsequent voltage-clamp recordings in hiAM-2.38 showed the presence of a strong Na^+ current (I_{Na}) and robust steady-state K^+ currents (**Supplemental Figure 12**), which were consistent with the fast upstroke velocity and haAM-like RMP of hiAM-2.38, respectively. Finally, a strong atrial-selective 4-AP (50 µM)-sensitive ultrarapid delayed rectifier K^+ current (I_{Kur}) was present in hiAMs, validating their atrial electrophysiological phenotype (**Supplemental Figure 12, Supplemental Table 4**). Overall, the electrophysiological properties of differentiated hiAMs strongly resemble those of primary human AMs.

Next, we assessed the conduction of APs in multicellular preparations by optical voltage mapping. Upon 1-Hz electrical point stimulation, cell layers (2-cm^2) of hiAM-2.38 displayed homogeneous conduction of APs (**Figure 4c,d**) with a CV of 24.4 ± 2.3 cm/s and APD_{80} of 136 ± 12 ms (**Figure 4e**), with APD restitution occurring at high activation frequencies (**Figure 4f**). Optical voltage mapping of hiAM-2.52 and hiAM-2.90 also showed homogeneous conduction of APs at speeds of 19.4 ± 2.0 cm/s and 11.9 ± 2.0 cm/s and with an APD_{80} of 129 ± 15 ms and 103 ± 9 ms, respectively (**Supplemental Figure 11**). Since confluent monocultures of hfAMs or haAMs could not be established because of shortage of source material, difficulties in removing the large percentage of non-cardiomyocytes from the starting material, minimal cardiomyocyte proliferation and/or poor cardiomyocyte survival, we used hESC-AMs for comparison. Due to limited production capacity of phenotypically homogenous hESC-AM populations, this comparison was performed in confluent 1-cm^2 cell layers. While hESC-AM layers had a high spontaneous beating rate consistent with their immature phenotype, spontaneous activity was rarely observed in hiAM-2.38 layers, but could be induced by chronotropic stimulation (**Supplemental Figure 13**). Following 1-Hz electrical point stimulation, conduction in hESC-AM layers appeared more heterogeneous and was > 10-fold slower compared with hiAM-2.38 layers of the same size (**Figure 4g-i, Supplemental Video 2**). In terms of optical AP characteristics, the optical upstroke time was longer in hESC-AMs compared with hiAM-2.38 (28 ± 6 vs. 12 ± 1 ms, $P < 0.001$, $n = 6$ and 7, respectively) while APD_{80} did not statistically differ between hESC-AMs and hiAMs. Similar differences in kinetics were found when comparing optically recorded Ca^{2+} transients between hESC-AM and hiAM-2.38 layers (**Supplemental Results, Supplemental Figure 14**).

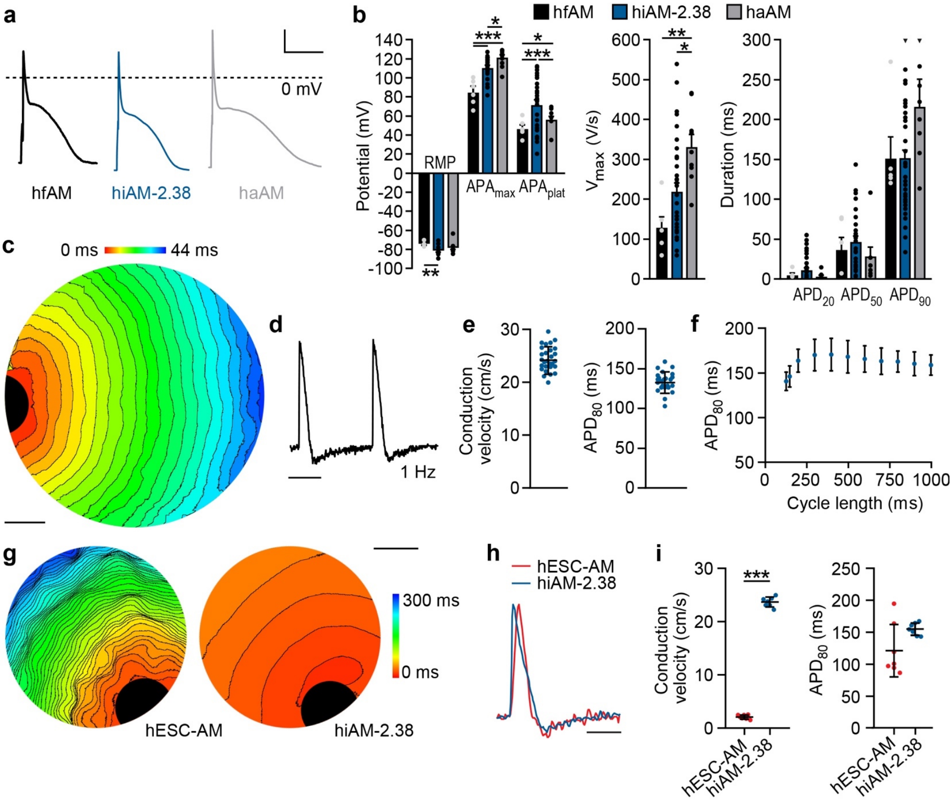

Figure 4. Electrophysiological characteristics of differentiated hiAMs. **(a)** Representative AP traces and **(b)** mean AP parameters of single hfAMs ($n = 6$ cells from 2 independent preparations), single differentiated hiAM-2.38 ($n = 39$ cells from 11 independent differentiations) and single haAMs ($n = 9$ cells) during 1-Hz electrical stimulation. APA_{max}, maximal AP amplitude. APA_{plat}, AP plateau amplitude. V_{max}, maximum AP upstroke velocity. $APD_{20/50/90}$, action potential duration at 20, 50 and 90% of repolarization. Scale bars in **(a)** x = 100 ms, y = 20 mV. The dotted line in **(a)** indicates the zero mV level. Data shown as mean with error bars indicating SEM. $^{**}P < 0.01$, $^{***}P <$

0.001, one-way analysis of variance with Tukey *post-hoc* analysis. **(c-f)** Optical voltage mapping of confluent layers of differentiated hiAMs in a 24-well format following 1-Hz electrical point stimulation. **(c)** Representative activation map of hiAM layer. Isochrones, 2 ms. Scale bar, 2 mm. **(d)** Representative optical voltage trace of hiAMs from **(c)**. Scale bar, 500 ms. **(e)** Mean CV and APD_{80} in confluent hiAM layers (n = 28 layers from 8 independent differentiations). Mean shown, with error bars indicating SD. **(f)** APD restitution curve of hiAM-2.38 (n = 10 layers from 2 independent differentiations). Mean shown, with error bars indicating SD. **(g-h)** Optical voltage mapping of confluent hESC-AM and differentiated hiAM-2.38 layers in a 48-well format. **(g)** Representative activation maps of hESC-AM and hiAM-2.38 layers. Isochrones, 6 ms. Scale bar, 2 mm. **(h)** Representative optical voltage traces from hESC-AMs and hiAMs of **(g)**. Scale bar, 250 ms. **(i)** Mean CV and APD_{80} during 1-Hz electrical stimulation in hESC-AM (n = 7 layers from 3 independent differentiations) and differentiated hiAM (n = 7 layers from 2 independent differentiations) layers. Mean shown, with error bars indicating SD. ***$P < 0.001$, unpaired t-test.

Robustness of hiAM differentiation

From the perspective of standardization, we assessed the robustness of hiAM differentiation. Massive expansion of hiAMs did not jeopardize their cardiomyogenic differentiation potential. Comparison of optical voltage mapping data of hiAM-2.38 that had undergone different PDs (between 28 and 46) before cardiomyogenic differentiation, revealed no significant change in average CV or APD_{80} (**Figure 5a, Supplemental Figure 15**). Also, no variation in structural characteristics as assessed by immunostaining for ACTN2 and TNNT2 was observed over this broad range of PDs (**Supplemental Figure 15**). Furthermore, repeatedly switching hiAMs back and forth between proliferation and differentiation did not noticeably alter their respective phenotypes. Specifically, the number of Ki-67-positive nuclei during proliferation, as well as the CV, APD_{80} and TNNT2 immunostaining pattern after differentiation were not affected by the repeated phenotypic transitions (**Figure 5b, Supplemental Figure 16**).

Next, we tested whether hard-to-control variations in the culture medium, such as the variable composition of foetal bovine serum (FBS) (21), would affect cardiomyogenic differentiation. The CV of hiAM cultures differentiated with 4 different sources of FBS did not significantly differ (**Figure 5b**). Similarly, no effect on APD_{80} was found, except that the premium FBS from USA origin had a minimal shortening effect on APD_{80} as compared to the FBS from South America, New Zealand and Brazil (**Figure 5b**). Finally, we investigated whether cryopreservation of differentiated hiAMs (in addition to cryopreservation of proliferating hiAMs) would be feasible. Thawing of hiAMs that had been cryopreserved at day 8 of differentiation, *i.e.* just before they exhibit contractions, resulted in 91.9 ± 1.6% of viable cells and an attachment efficiency of 70.4 ± 5.2% (**Figure 5c**). Following 6 additional days of culture in supplemented differentiation medium to complete cardiomyogenesis, the hiAM layers did not show significant differences in electrophysiological characteristics when compared to control layers established with hiAMs that had not been cryopreserved in a partially differentiated state (**Figure 5d**). Together, these data demonstrate robust hiAM differentiation irrespective of passage history, culture conditions or intermediate cryopreservation.

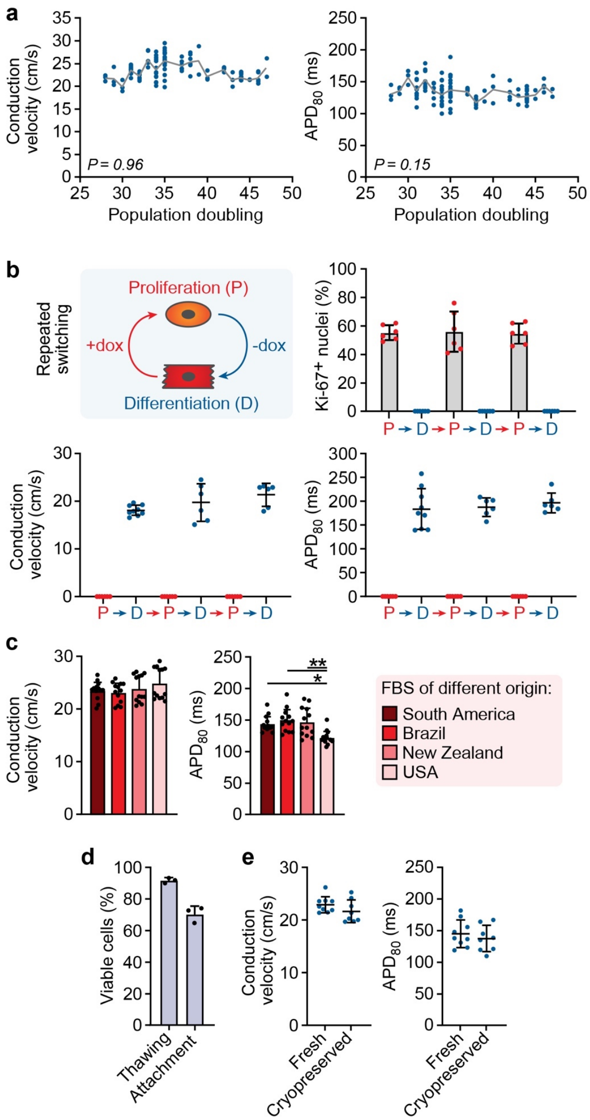

Figure 5 (legend on next page).

Figure 5 (previous page). Robustness and effect of cryopreservation on hiAM differentiation capacity. **(a)** CV and APD_{80} of hiAM-2.38 layers measured using optical voltage mapping over a broad range of PDs ($n = 111$). Stability of mean CV and APD_{80} at various PDs was tested using the Pearson correlation coefficient. **(b)** Percentage of hiAM-2.38 with Ki-67-positive nuclei determined by immunocytochemistry and CV and APD_{80} of hiAM-2.38 measured by optical voltage mapping during repeated switching between proliferation (P) and differentiation (D). $n = 6$-9 layers per time point from 3 independent experiments. **(c)** Electrophysiological characteristics of hiAM-2.38 layers following differentiation using FBS of various origins and suppliers: South America (standard serum, S1860, Biowest), Brazil (10270098, Thermo Fisher Scientific), New Zealand (A3160901, Thermo Fisher Scientific) and USA (Premium FBS, 16000036, Thermo Fisher Scientific; $n = 13$ layers per group from 3 independent differentiations). $^{*}P < 0.05$, $^{**}P < 0.01$, one-way analysis of variance with Tukey *post-hoc* analysis. **(d)** Viability (determined by the Trypan Blue dye exclusion test) and attachment efficiency after thawing of hiAMs that had been cryopreserved at day 8 of differentiation ($n = 3$ batches each comprising 3 vials with 10^6 hiAMs per vial). **(e)** Electrophysiological characteristics using optical voltage mapping of freshly differentiated hiAM-2.38 ($n = 9$ layers from 3 independent differentiations) *vs.* cryopreserved differentiated hiAM-2.38 layers ($n = 8$ layers from 3 independent differentiations). **(b-e)** Mean shown, with error bars indicating SD.

hiAMs as atrial arrhythmia model

We next investigated the suitability of hiAMs for AF modelling. As induction of reentry in hiAM layers was not feasible in the 2-cm^2 format and the average area of reentrant circuits in human AF is ~3 cm^2 (22,23), we used 10-cm^2 confluent hiAM layers to provide space for multiple reentrant circuits. hESC-AM layers of 1 cm^2 were included for comparison, because of the aforementioned difficulty to establish larger confluent monolayers of these cells. Upon high-frequency electrical point stimulation, arrhythmic activity with varying degrees of complexity could be induced in both 1-cm^2 hESC-AM and 10-cm^2 hiAM layers (**Figure 6a,b, Supplemental Video 3**). Reentrant activity induced in hESC-AM layers had an average activation frequency of 3.0 ± 0.8 Hz, which was consistent with previous reports of arrhythmic hESC-AM layers (24). In hiAM-2.38 layers, however, the average activation frequency was significantly higher (7.5 ± 1.0 Hz, **Figure 6c**). Also in hiAM-2.52 and hiAM-2.90 layers, reentrant activity with high activation frequencies could be induced (7.2 ± 0.8 and 7.9 ± 0.6 Hz, respectively, **Supplemental Figure 17**). Interestingly, these activation frequencies very closely resemble those previously measured in the clinic in AF patients (25-27). As expected from the faster CV in hiAM layers, reentrant circuit wavelength was greater in hiAM-2.38 layers than in hESC-AM layers (**Figure 6d**). As a result, the arrhythmia complexity (expressed as number of reentrant circuits per cm^2) was higher in hESC-AM layers compared to hiAM-2.38 layers (**Figure 6e, Supplemental Video 4**). Similar data were obtained in arrhythmic hiAM-2.52 and hiAM-2.90 layers (**Supplemental Figure 17**). Moreover, in hESC-AM layers, the cycle length of reentrant circuits was much longer than the baseline APD_{80}, whereas in hiAMs these two parameters were very similar (**Figure 6f**). Thus, reentrant circuits in hESC-AMs displayed a large temporal excitable gap compared to nearly no gap in hiAMs (**Supplemental Figure 17**), which suggests that the slow CV in hESC-AM layers might be responsible for the low activation frequencies. Overall, hiAM monolayers better recapitulate the dynamics of human AF than hESC-AM monolayers.

Effects of traditional antiarrhythmic drugs in hiAM-based AF model

The applicability of the hiAM-based AF model to study pharmacological interventions was tested using sotalol and flecainide, two antiarrhythmic drugs commonly used for rhythm control in AF patients (28-30). Dimethylsulfoxide (DMSO), which served as solvent/vehicle for flecainide, did not affect the CV or APD in hiAM-2.38 layers subjected to 1-Hz electrical point stimulation. Increasing concentrations of sotalol had also no effect on CV, but did dose-dependently increase the APD_{80} (**Figure 7a, Supplemental Figure 18**), as would be expected by its strong inhibitory effect on the rapid delayed rectifier K^+ current (I_{Kr}) (31). Flecainide, which mainly inhibits I_{Na} and I_{Kr} (32), decreased the CV and prolonged the APD_{80} in a dose-dependent matter. For each compound, 3 incremental doses were selected (DMSO: 0.01, 0.03 and 0.1%; Sotalol: 3, 10 and 30 μM; Flecainide 1, 3 and 10 μM), including clinically relevant concentrations (**Figure 7b**).

Following the induction of stable reentry in hiAM-2.38 cultures, slow infusion of DMSO rarely resulted in termination of reentrant activity (**Figure 7c,d**). DMSO also did not significantly alter the activation frequency, with the exception of the 0.01% dose which slightly reduced the frequency (**Figure 7e**). Sotalol infusion resulted in sporadic termination of reentrant activity, although for none of the doses termination rates significantly differed from those caused by DMSO treatment. The activation frequency, however, was significantly reduced for all sotalol concentrations in a dose-dependent manner. Finally, infusion of flecainide did result in frequent arrhythmia termination at the two highest doses and also significantly reduced the activation frequency in a dose-dependent manner. These observations were also confirmed in hiAM-2.52 and hiAM-2.90 cultures (**Supplemental Figure 19**). For these clones, 0.1% DMSO did not terminate any reentrant activity, whereas 10 μM flecainide resulted in frequent reentry termination. Thus, using the hiAM-based AF model, we were able to recapitulate the effects exerted by common antiarrhythmic drugs in AF patients at clinically relevant activation frequencies (**Supplemental Video 5**).

Figure 6 (legend on next page).

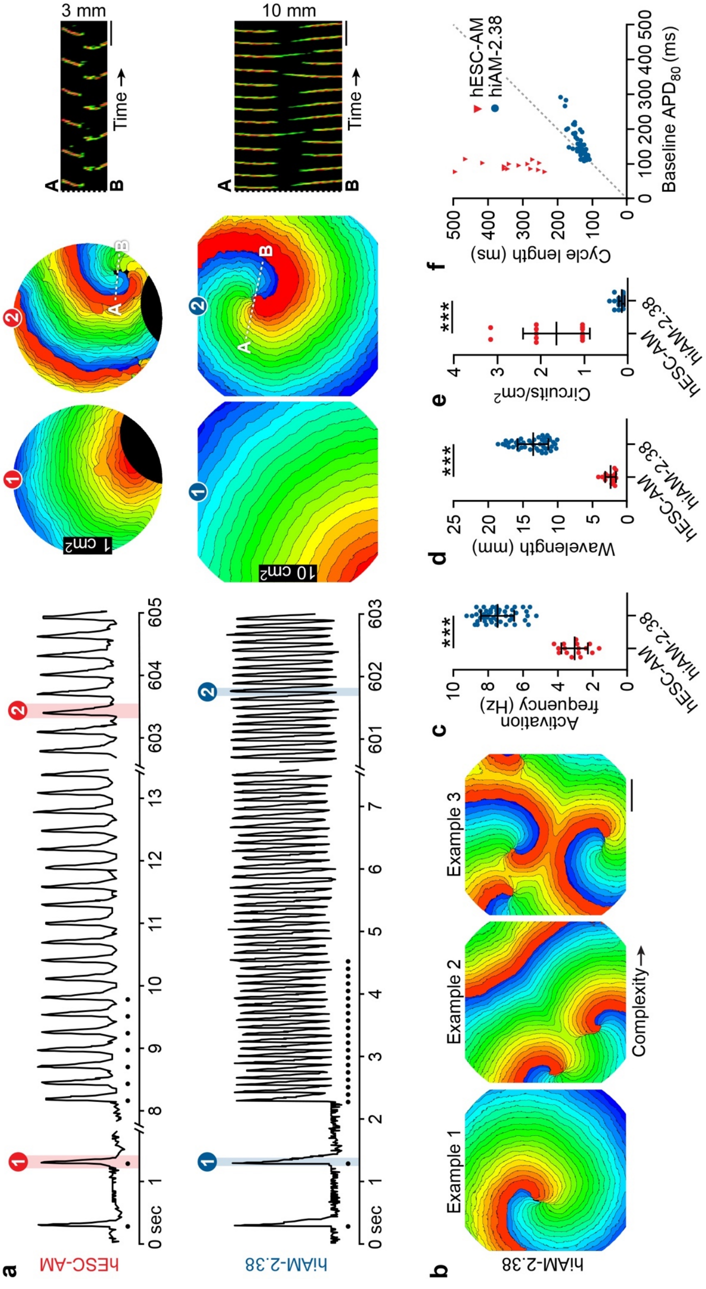

Figure 6 (previous page). hESC-AM- and hiAM-based atrial arrhythmia models. **(a)** Optical voltage traces of reentrant circuit induction by high frequency electrical pacing in 1-cm^2 hESC-AM and 10-cm^2 differentiated hiAM cultures (left). Corresponding activation maps before and after arrhythmia induction (middle). Line scan analysis between points A and B assessing reentrant circuit stability (right). Dots above the axes represent time points of electrical stimulation. Isochrones, 12 ms (hESC-AMs), 6 ms (hiAMs). Scale bar, 250 ms. **(b)** Example of three 10-cm^2 hiAM-2.38 cultures following induction of reentrant activity of increasing complexity, *i.e.* with an increasing number of reentrant circuits. Isochrones, 6 ms. Scale bar, 5 mm. **(c)** Mean activation frequency of hESC-AM and hiAM cultures following induction of reentrant circuits. **(d)** Mean wavelength of reentrant circuits. **(e)** Arrhythmia complexity following stabilization expressed as number of reentrant circuits per cm^2. **(f)** Correlation between baseline APD_{80} and cycle length of induced reentrant circuits in hESC-AM and hiAM cultures. **(c-e)** Mean shown, with error bars indicating SD. ***$P < 0.001$, unpaired *t*-test. **(c-f)** hESC-AM: $n = 16$ arrhythmia episodes from 7 independent cultures, hiAM-2.38: $n = 56$ independent cultures.

Figure 7 (next page). Effects of antiarrhythmic drugs in the hiAM-based atrial arrhythmia model. **(a)** Effects of various concentrations of DMSO (solvent/vehicle control), sotalol or flecainide on CV (red, left axis) and APD_{80} (blue, right axis) in differentiated 2-cm^2 hiAM-2.38 cultures ($n = 5$ cultures for each compound). Repeated measured analysis of variance with Tukey *post-hoc* analysis. **(b)** Representative optical voltage traces of differentiated hiAM-2.38 in the presence of various concentrations of DMSO, sotalol or flecainide. Scale bar, 100 ms. **(c)** Representative optical voltage traces of arrhythmic hiAM-2.38 cultures before and after infusion of DMSO (0.1%), sotalol (30 μM) or flecainide (10 μM). Dots above the lower axis represent time points of electrical stimulation. **(d)** Rate of reentrant circuit termination in arrhythmic hiAM-2.38 cultures at 10 min after infusion of DMSO, sotalol or flecainide. The termination rates at the different sotalol and flecainide concentrations were compared with the termination rate of the combined DMSO concentrations using the Chi-square test. **(e)** Change (Δ) in activation frequency in arrhythmic hiAM-2.38 cultures following DMSO, sotalol or flecainide infusion (baseline compared to 10 min after infusion or prior to termination). Paired *t*-test. **(f)** Continuous monitoring of mean activation frequency in arrhythmic hiAM-2.38 cultures prior to and after infusion of compounds at the indicated concentrations. **(c-f)** Additional details on arrhythmia dynamics and termination mechanisms following drug infusion are provided in **Supplemental Figure 20.** **(d-f)** n = 8-10 experiments for each dose, from 57 independent cultures. **(a, e)** Mean shown, with error bars indicating SD. **(a, d, e)** *$P < 0.05$, **$P < 0.01$, ***$P < 0.001$.

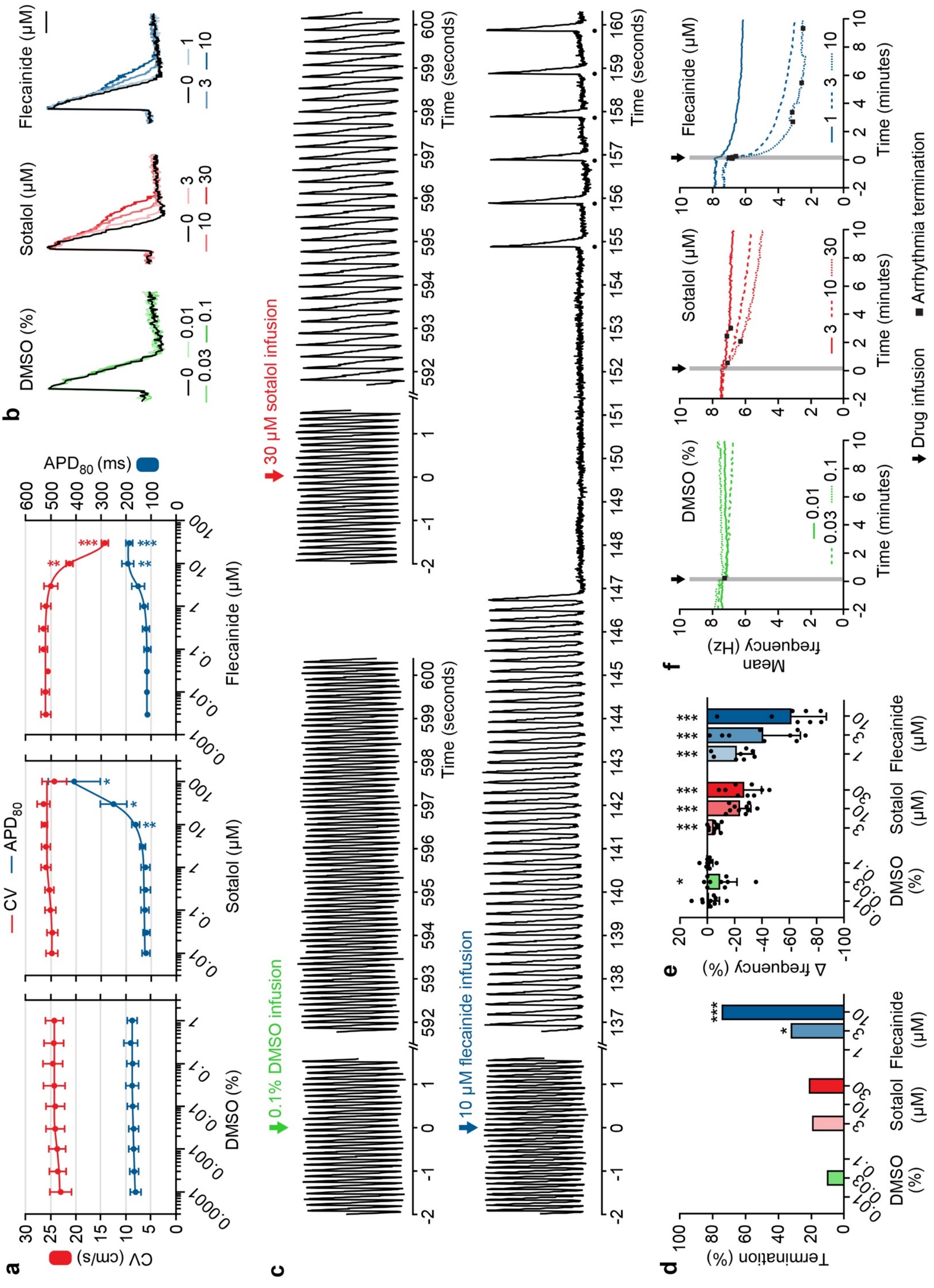

Figure 7 (legend on previous page).

Discussion

Preclinical biomedical research across academia and industry has created a large demand for difficult to obtain human parenchymal cells to increase pathophysiological insight and develop novel therapeutics. Although recent progress in human pluripotent stem cell (hPSC) technology has greatly advanced the development of human disease models, several challenges remain regarding their scalability, representativeness and reproducibility. To address these issues, we developed an LV-based method for the conditional immortalization of primary mammalian cells. In this study, we describe the generation of standardized lines of human AMs with preserved cardiomyogenic differentiation capacity as a demonstration of the efficacy of this method. These so-called hiAM lines display strict control over proliferation and differentiation, allowing massive (*i.e.* quadrillion-fold) cell expansion followed by differentiation towards fully functional (*i.e.* excitable and contractile) human AMs. The generation of these differentiation-competent human cardiomyocyte lines enabled the creation of human AF models that featured fibrillatory activity at clinically relevant frequencies, which could be terminated using antiarrhythmic drugs used in clinical practice.

The development of human cardiac muscle cell lines with preserved cardiomyogenic differentiation capacity has been the scope of several studies over the last decades (33,34). Thus far, human cardiomyocyte lines failed to recapitulate the structural and functional characteristics of the primary cells from which they were derived. Here, we show that this shortcoming can be overcome by imposing stringent control over SV40 LT expression in the target cells. The resulting hiAM lines allow straightforward production of contractile and excitable AMs in quantities not conceivable heretofore (*e.g.* one hiAM line can generate the number of cardiomyocytes present in 100,000 human adult hearts). Due to the monoclonal nature of hiAM lines and the high efficiency with which the cells undergo cardiomyogenic differentiation, pure populations of human AMs can be produced with great ease. This provides a clear advantage over derivation of AMs from hPSCs, which is a rather laborious and time-consuming multiphase process that generally includes a purification step (35,36) to select against the non-AMs remaining with current differentiation protocols (24,37,38). Moreover, differentiation completely abolishes proliferation of hiAMs while hPSC-derived cardiomyocytes still display some residual mitotic activity (39,40). Additionally, our comparative transcriptome analyses show that differentiated hiAMs closer match the gene expression profile of haAMs than hESC-AMs. Also, hPSC-AMs from different studies have a non-physiological average RMP of approximately -56 mV, reflecting their immature electrophysiological phenotype (24,37,38,41). Differentiated hiAMs, on the other hand, display an average RMP of -79 mV, which is well within the -70 to -85 mV range reported for haAMs (42-44). The depolarized membranes of hPSC-AMs likely contribute to the slow AP propagation observed in confluent 2/3D cultures of these cells (24,45,46). Above -70 mV, a considerable fraction of Na^+ channels becomes inactivated, resulting in a decrease of AP upstroke velocity and a consequential reduction of CV. Although the CV in hiAM layers is significantly faster than in layers of hPSC-AMs (up to 30 cm/s vs. up to 2.5 cm/s), it is still slower than the 60-75 cm/s reached in human adult atrial tissue (47). This can, at least in part, be explained by the absence of anisotropic organization and neurohumoral regulation in the monolayers of differentiated hiAMs (48), providing a rationale for the future application of *in vitro* patterning technology to create cables/sheets of uniaxially aligned hiAMs and thereby increase the (longitudinal) CV in these structures along with neurohormonal stimulation.

The basic electrophysiological properties of hiAMs and hPSC-AMs also directly influence their applicability for AF modelling. The first report (24) of reentrant circuit induction in (non-purified) hESC-AM layers showed activation at a mean frequency of 3.2 Hz, which is very similar to the 3.0 Hz we found in our (purified) hESC-AM layers, but much lower than the 7.5 Hz in hiAM layers. For reference, activation frequencies measured in AF patients range between 6 to 8 Hz, depending on the type of AF (25-27). When studying the influence of antiarrhythmic drugs on reentry dynamics, activation frequencies resembling clinical AF are critical because of (reverse) rate-dependent effects. For instance, the I_{Na}-blocking activity of flecainide is increased at higher activation frequencies (49), which could explain why termination of reentry using 10 µM flecainide was possible in the majority of hiAM layers, while this was previously not successful in hESC-AM layers (24). As our hiAM-based AF model displays the main electrophysiological phenomena driving AF and provides new possibilities over existing models for studies into arrhythmia dynamics and antiarrhythmic drug discovery, a future extension would be to move towards more advanced 3D *in vitro* models of AF. Atrium-like 3D tissues have recently been generated using hPSC-AMs (46,50,51), but due to their small size (largest dimension ≤ 5 mm) they cannot accommodate reentrant circuits with characteristics similar to human AF. Advances in bioprinting technology have already demonstrated the feasibility of creating large and complex (cardiac) scaffolds required for tissue engineering of whole human hearts (52). The main limiting factor for the creation of such large tissue constructs to date, has been the difficulty associated with generating the hundreds of millions/billions of well-differentiated cells necessary to populate these constructs. Although a recent report has shown that this problem may at least be partially overcome by a new method allowing the expansion of hiPSC-derived ventricular myocytes (40), it remains to be seen whether it can also induce multiplication of hPSC-AMs. Accordingly, the extensive scalability, cost-effectiveness and robustness of hiAM differentiation might provide a new impulse to create larger human atrial constructs for disease modelling, mechanistic studies and drug screening.

The ability to generate large numbers of differentiated hiAMs in an effective and robust manner may furthermore open the possibility to use them for biopharmaceutical production of, for instance, cardiomyocyte-derived exosomes and cardiokines (53). The latter property together with the monoclonal origin of hiAMs and the high controllability of their phenotype and gene expression profile, makes these cells particularly suitable for (very) high-resolution "omics" studies by obviating the need for cell selection and by providing plentiful input material. This offers new possibilities 1) to identify yet unknown factors involved in cardiomyocyte proliferation and differentiation, and 2) to find novel therapeutic targets, especially when combined with (opto)genetic, pharmaceutical, chemical or physical interventions to mimic disease states.

Although hiAM lines have many advantages over current AM sources, their suitability for regenerative purposes is limited due to the use of an integrating LV encoding an oncoprotein (*i.e.* SV40 LT) for (conditional) immortalization, which harbours the risk of tumour formation. hiAMs may, however, still be applied in animal models to optimize cardiac cell therapy, and may help to find new leads for endogenous induction of myocardial regeneration through stimulation of cardiomyocyte proliferation *in situ*. Although the high controllability and synchronicity of the transition from proliferation to differentiation could make hiAMs an excellent model for studying the molecular mechanisms underlying this transition, they will not fully represent the natural course of events due to the very nature (*i.e.* viral oncoprotein-dependent conditional immortalized state) of the cells. Moreover, the aneuploid status of hiAMs, which is associated with expression of SV40 LT (54), might limit certain applications with high sensitivity to potential gene imbalances. Nevertheless, this status did not result in apparent deviations from the AM phenotype based on our comprehensive comparative analyses. In addition, the initial investment associated with the development of these cell lines, as well as the need for access to primary cardiac material, makes the conditional immortalization technique less suited than hiPSC technology for widescale patient-specific disease modelling. Still, using gene delivery or genome editing technologies, hiAM sublines with genetic modifications could easily be created, allowing studying the effects of these alterations in a highly standardized cell system. For instance, as described in the **Supplemental Results**, we could show that differentiated hiAMs with lentiviral short hairpin RNA-mediated knockdown of TBX5 expression display very similar disturbances of Ca^{2+} dynamics as observed in Holt-Oram syndrome (**see Supplemental Figure 21**). The ease with which hiAMs can be genetically modified makes it possible to perform comprehensive mechanistic studies mimicking the different types of atrial disease (55), allowing dissection of the precise molecular signatures of the diverse atrial cardiomyopathies, fostering thereby the development of novel preventive anti-AF therapies.

In summary, the conditional immortalization of hfAMs has enabled the creation of 1) the fully differentiation-competent lines of human cardiomyocytes and 2) human *in vitro* models of AF displaying clinically relevant features, which can be readily genetically modified to also mimic specific inherited atrial cardiomyopathies. This provides proof-of-concept of a versatile new method to produce, in a simple and rapid manner, massive numbers of authentic human cells for the development of representative human *in vitro* models for animal-free disease investigation, target identification along with drug discovery and therapeutic testing.

Methods

LV production

To generate vesicular stomatitis virus G protein-pseudotyped LV.iMHCK7.LT-WT particles, near confluent monolayers of 293T cells (56) were transfected with LV shuttle construct pLV.iMHCK7.LT-WT (**Supplemental Figure 1**) and the packaging plasmids psPAX2 (Addgene, plasmid number: 12260) and pLP/VSVG (Thermo Fisher Scientific, K497500) at a molar ratio of 2:1:1. pLV.iMHCK7.LT-WT is identical to pLV.iMHCK7.LT-tsA587 except for the replacement of the coding sequence of the temperature-sensitive SV40 LT mutant tsA58 by that of wild-type LT. The 293T cells were cultured in high-glucose Dulbecco's modified Eagle's medium (DMEM, Thermo Fisher Scientific, 41966) with 10% FBS (Thermo Fisher Scientific, 10270-106). The transfection mixture, consisting of 35 µg of plasmid DNA and 105 µg of linear 25-kDa polyethyleneimine (Polysciences, 23966) in 2 mL of 150 mM NaCl per 175-cm^2 cell culture flask (Greiner Bio-One, 660160), was directly added to the culture medium. Approximately 16 h later, the transfection medium was replaced by 15 mL of fresh high-glucose DMEM supplemented with 5% FBS and 25 mM HEPES-NaOH (pH 7.4). At ~48 h after the start of the transfection procedure, the culture supernatants were collected, cleared from cellular debris by centrifugation at room temperature (RT) for 10 min at 3,750×*g* and subsequent filtration through 0.45-µm pore-sized, 33-mm diameter polyethersulfone Millex-HP syringe filters (Merck Millipore, SLHP033RB). The LV particles were further purified and concentrated by underlaying 30 mL of vector suspension in a 38.5-ml polypropylene ultracentrifuge tube (Beckman Coulter, 326823) with 5 mL of 20% (wt/vol) sucrose in phosphate-buffered saline (PBS) and subsequent centrifugation for 2 h at 4°C with slow acceleration and without braking at 15,000 revolutions per min in an SW32 rotor (Beckman Coulter, 369650). Next, the supernatants were discarded and each pellet was suspended in 500 µl of PBS-1% bovine serum albumin (Sigma-Aldrich, A2153) by overnight incubation with gentle shaking at 4°C. The concentrated vector suspension was divided on ice in 100 µl aliquots for storage at -80°C.

Ethics Statement

Human foetal cardiac samples were obtained after elective abortions and with written informed consent. Donors were not incentivised/compensated. The samples were delivered to the researcher without any information except for the age of the foetus to guarantee full anonymity of the donors. This study was conducted with approval of the institutional review board of the Leiden University Medical Centre (P08.087) and in compliance with the International Code of Medical Ethics of the World Medical Association.

Isolation and culture of hfAMs

The atria were separated from the ventricles of the foetal heart, minced into pieces of ~1 mm^2 and dissociated by 2 successive 30-min treatments with collagenase type I (225 U/ml, Worthington Biochemical, LS004196) and DNase I (20 U/ml, Sigma-Aldrich, DN25) under gentle agitation at 37°C. Cells were pelleted by centrifugation for 10 min at 160×*g* and RT. The supernatant was removed and cells were resuspended in Ham's F10 medium (Thermo Fisher Scientific, 11550) supplemented with 100 units/mL of penicillin and 100 µg/mL of streptomycin (Thermo Fisher Scientific, 15070-063), 10% heat-inactivated FBS (Thermo Fisher Scientific, 10500) and 10% heat-inactivated horse serum (Thermo Fisher Scientific, 26050). The cell suspension was transferred to uncoated Primaria culture dishes (Corning, 353803) and incubated for 75 min at 37°C in a humidified atmosphere of 95% air-5% CO_2 to allow preferential attachment of non-cardiomyocytes. Unattached cells were filtered through a nylon cell strainer (Corning, 431751) containing evenly spaced 70-µm mesh pores and seeded for experiments. For conditional immortalization, 10^4 cells/cm^2 were seeded in a 6-well culture plate (Corning, 3506) coated with fibronectin from bovine plasma (100 µg/mL, Sigma-Aldrich, F1141). For immunocytochemistry and patch-clamping, respectively 5×10^4 and 2.5×10^4 cells/cm^2 were seeded on fibronectin-coated glass coverslips in 24-well plates (Corning, 3524).

Conditional immortalization and selection of hiAM monoclones

The human foetal atrial cell mixture was transduced with 2.5 µl of concentrated LV.iMHCK7.SV40-LT-WT stock (*i.e.* the vector yield of 1.65×10^5 producer cells), following 2 days of recovery. Three days following transduction, the culture medium was changed to hiAM proliferation medium, consisting of Advanced DMEM/F-12 (Thermo Fisher Scientific, 12634), 2 mM GlutaMAX (Thermo Fisher Scientific, 35050061), 2% FBS (Biowest, S1810), 100 units/mL of penicillin and 100 µg/mL of streptomycin supplemented with 100 ng/ml doxycycline hyclate (Sigma-Aldrich, D9891) to induce SV40 LT expression. After the observation of cell proliferation, cells were detached using Accutase (BD Biosciences, 561527) and plated at a density of 10 cells/cm^2 in 145-mm diameter culture dishes (Greiner Bio-One, P7737) in the presence of hiAM proliferation medium. These dishes were maintained for 2-3 weeks at 37°C in a humidified atmosphere of 95% air-5% CO_2 until colonies of 100-200 cells were observed. Individual colonies were then isolated with the aid of glass cloning cylinders (⌀ 6 mm, Corning, 3166-6) and treated with Accutase, after which the collection of cells inside each cylinder was transferred to single wells of a 48-well plate (Corning, 3548) in hiAM proliferation medium. Isolated colonies were given a unique number, expanded up to 106 cells and graded based on their proliferative and differentiation qualities. The conditional immortalization was considered successful for hiAM monoclones that 1) when given dox-containing hiAM proliferation medium proliferated beyond 15 PDs with a PD time shorter than 120 h and 2) in the presence of dox-free hiAM differentiation medium (see below) a) stopped proliferating and gradually acquired a cardiomyocyte-like phase-contrast appearance, b) lost proliferation marker Ki-67 expression and eventually consisted of > 50% of TNNT2-positive cells as assessed by immunocytochemistry and c) were electrically excitable with a minimal CV of 10 cm/s and maximal APD80 of 300 ms following optical voltage mapping of 1-cm^2 monolayers ≥ 12 days after dox removal. All selection criteria, including corresponding drop-off rates per criterium, can be found in **Supplemental Figure 1**.

Proliferation and differentiation of hiAMs

Proliferating hiAMs were cultured in uncoated TC-treated CELLSTAR flasks (Greiner Bio-One, 6901755, 658175, 660175) in the aforementioned hiAM proliferation medium. Culture medium was refreshed every 2-3 days. When confluency approached 90%, proliferating hiAMs were subjected to a 10-min treatment with Accutase at 37°C and carefully triturated into a (nearly) single-cell suspension. Next, the cells were pelleted by centrifugation for 5 min at 160×*g* and RT and transferred in a 1:2 to 1:4 ratio to new culture flasks for further multiplication, or seeded in appropriate culture plates for cardiomyogenic differentiation. Differentiation of hiAMs was performed in fibronectin-coated culture plates and initiated by changing the hiAM proliferation medium to hiAM differentiation medium, consisting of Advanced DMEM/F-12 (Thermo Fisher Scientific, 12634), 2 mM GlutaMAX and 2% Biowest FBS. Starting at day 4 of differentiation (the initiation of differentiation being day 0), hiAM differentiation medium was supplemented with 20 ng/ml triiodo-L-thyronine (T3) hormone (Sigma-Aldrich, T6397), 400 ng/ml dexamethasone (Centrafarm, 55091), 8 µM LF3 (Selleck Chemicals, S8474) or 10 µM ICRT14 (Sigma-Aldrich, SML0203) and 10 µM phenylephrine (Sigma-Aldrich, P6126).

Culture medium was refreshed every 2 days during differentiation. At day 12 of differentiation, the hiAMs were considered fully differentiated as at that time point CV and APD reached their plateau values. All experiments in this study were performed between day 12 to 15 after initiation of differentiation.

Proliferation assay

To assess the proliferation rates of individual hiAM clones in the presence of dox, 2×10^3 cells/cm^2 were seeded in multiple 100-mm diameter culture dishes (Corning, 430167). At 48-h intervals following culture initiation, cells were detached using Accutase, collected in hiAM proliferation medium and mixed in a 1:1 ratio with 0.4% Trypan Blue (Sigma-Aldrich, T8154). Following brief incubation, cells were counted using a CytoSMART Cell Counter (Corning). PD times were calculated by fitting data with an exponential growth equation (GraphPad Prism, v8.0.1, GraphPad Software).

Immunocytochemistry and image quantification

hfAMs and hiAMs were seeded at a density of 8×10^4 cells/cm^2 on fibronectin-coated coverslips prior to fixation with 4% buffered formaldehyde (Added Pharma, 14144751) for 30 min at 4°C. Cells were permeabilized by incubation with PBS/0.1% Triton X-100 (Sigma-Aldrich, X100) for 10 min, incubated with PBS/10% normal donkey serum (NDS, Sigma-Aldrich, D9663) for 30 min to block non-specific background staining and subsequently exposed to the primary antibody in PBS containing 0.5% NDS for 2 h, all at RT. After each treatment, cells were washed 3 times with PBS. Secondary antibody incubation was performed in PBS containing 0.5% NDS for 45 min and nuclei were stained for 10 min with Hoechst 33342 solution (Thermo Fisher Scientific, H-3570) diluted 1:1000 in PBS. For an overview of the antibodies and the dilutions at which they were applied, see **Supplemental Table 5**. Coverslips were mounted on StarFrost slides (VWR International, KNITVS112731FEA.01) using VECTASHIELD (Vector Laboratories, H-1000-10) and imaged with an Eclipse 80i Upright Microscope (during clone screening, Nikon Instruments) or TCS SP8 White Light Laser Confocal Microscope (during characterization, Leica Microsystems). Details on the use of the fluorescence microscopes are provided in the **Supplemental Methods**.

Counting of Ki-67-positive nuclei on the basis of mean grey values was performed using ImageJ (v1.52a, http://imagej.nih.gov/). For hiAMs, all Hoechst 33342-positive nuclei were analysed. In the case of the primary hfAMs, only the Nkx-2.5-positive nuclei were considered to avoid analysis of the non-cardiomyocytes present in the samples. The mean grey value of each nucleus was compared to a threshold to distinguish between positive and negative nuclei. Sarcomere length was calculated by measuring the z-line distance of multiple adjacent sarcomeres in cell layers stained for ACTN2 (LAS X, v3.6.0, Leica Microsystems).

Western blotting

Adherent hiAMs were lysed on ice in RIPA buffer (50 mM Tris-HCl [pH 8.0], 150 mM NaCl, 1% NP-40, 0.5% sodium deoxycholate, 0.1% sodium dodecyl sulfate) supplemented with Roche cOmplete Mini Protease Inhibitor Cocktail (Sigma-Aldrich, 4693124001). The lysate was passed 3 times through a 30-gauge needle (BD Biosciences, 324826), centrifuged for 20 min at 4ºC and 16.000×*g*, after which the supernatant was collected and stored at -80ºC. Protein concentrations in the cleared lysates were determined using the Pierce BCA Protein Assay Kit (Thermo Fisher Scientific, 23225). Proteins were size-fractionated in Invitrogen Bolt 10% Bis-Tris Plus gels (Thermo Fisher Scientific, NW00102BOX) and transferred to Amersham Hybond P 0.45-μm polyvinylidene difluoride membranes (GE Healthcare, GEHE10600023) by wet electroblotting using a Bolt Mini Blot Module (Thermo Fisher Scientific). Membranes were incubated for 1 h in 2% ECL Prime blocking reagent (GE Healthcare, RPN418) dissolved in Tris-based saline/0.1% Tween 20 (TBST). Membranes were then incubated for 1 h with the primary antibody in TBST/2% ECL Prime blocking reagent, washed 5 times with TBST and incubated for 1 h with corresponding horseradish peroxidase-conjugated secondary antibodies. Information about the antibodies used can be found in **Supplemental Table 5**. Following 5 washes with TBST, membranes were covered with SuperSignal West Femto Maximum Sensitivity Substrate (Thermo Fisher Scientific, 34095) and chemiluminescence was measured using the ChemiDoc Touch Imaging System (Bio-Rad Laboratories) or iBright FL1500 Imaging System (Thermo Fisher Scientific). In some cases the blot was stripped following imaging using Restore PLUS Western Blot Stripping Buffer (Thermo Fisher Scientific, 46430) for an additional round of immunostaining. Protein levels were quantified with the aid of Image Lab (v6.0.1, Bio-Rad Laboratories) or the on-instrument software of the iBright FL1500 Imaging System, using levels of the housekeeping proteins and loading controls glyceraldehyde 3-phosphate dehydrogenase (GAPDH) or lamin A/C (LMNA) for normalization purposes.

RNA-sequencing hiAM proliferation vs. differentiation

Total RNA was extracted from proliferating and differentiated hiAMs seeded at a density of 10^5 cells/cm^2 (10^6 cells per sample) using the RNeasy Plus Mini Kit (Qiagen, 74104) according to manufacturer's instructions. RNA-sequencing was performed by GenomeScan (Leiden, the Netherlands). Quality and integrity of the RNA were confirmed using a 2100 Bioanalyzer Instrument (Agilent Technologies), with a measured RNA quality number of 10.0 for all samples. Library preparation was performed using the NEBNext Ultra II Directional RNA Library Prep Kit for Illumina in combination with the NEBNext Poly(A) mRNA Magnetic Isolation Module (New England Biolabs, E7765). Sample quality and yield after cDNA synthesis and polymerase chain reaction enrichment were measured with the bioanalyzer (range average size 445-524 base pairs [bp]). Clustering and DNA sequencing (50-82 million 150-bp paired-end reads) using the NovaSeq6000 DNA sequencer (Illumina) was performed according to manufacturer's protocols. Image analysis, base calling and quality check were performed with the Illumina data analysis pipeline RTA3.4.4 and Bcl2fastq (v2.20). Prior to alignment, the reads were trimmed for adapter sequences using Trimmomatic (v0.30). Reads were aligned to the Homo sapiens reference genome (GRCh37.75) using Tophat (v2.0.14) and read counts were determined using HTSeq (v0.6.1p1). Additionally, TPM values were calculated to compare gene expression levels between groups. Differential gene expression (Wald test) was assessed by analysing read counts with the DESeq2 package (v1.14.1) in the R platform (v3.3.0). Genes with an absolute log2-fold change > 1.0 (*i.e.* a > twofold absolute change) and false discovery rate (FDR)-corrected $P < 0.001$ were considered differentially expressed. Comparison of differentially expressed genes (DEGs) between clones was limited to genes with > 1 TPM in the proliferative state or at day 12 of cardiomyogenic differentiation to exclude DEGs with very low overall expression. Gene set enrichment analysis was performed in DAVID (v6.8).

RNA-sequencing hESC-AMs and hiAMs

Total RNA was extracted from hESC-AMs (10^6 cells per sample) using the NucleoSpin RNA kit (Macherey-Nagel, 740955) according to manufacturer's instructions. Total RNA extraction from hiAMs has been described above. Libraries were generated from 200 ng RNA using the KAPA-RNA HyperPrep kit with RiboErase (Roche, 8098131702) to remove ribosomal RNA, according to manufacturer's instructions. Library amplification was performed with 11 cycles, after which the size distribution was determined with a 2100 Bioanalyzer Instrument. Paired-end library sequencing was performed with the

NextSeq500 sequencing system (Illumina). Trimming of the reads and alignment was performed with seq2science (v0.4.0, available on Zenodo, https://doi.org/10.5281/zenodo.4451349). In short, Fastp (57) (v0.20.1) trimmed the low quality 3' ends and Salmon (58) (v1.3.0) quant aligned the reads to the GRCh38.p13 genome from Ensembl, after which tximeta (59) (v1.4.3) generated the gene expression matrix. The counts per million (CPM) were log1p-transformed. The published foetal dataset by Cui et al. (19) was retrieved as count matrix and the mean of expression was calculated per tissue type. The 2000 most variable genes within this dataset were determined with the variance-stabilized transformation method in Seurat (60) (v3). The selection of most variable genes in the GTEx portal dataset (20) was performed by taking the genes with a coefficient of variation > 2. Differential gene expression analysis (Wald test) between hESC-AMs and hiAMs was performed with the R package DESeq2 (61) (v1.22.2). The differential gene list was filtered for a log2-fold change > 1 and *P*-adjusted value < 0.01 (4145 significant differential genes in total), and visualized with pheatmap (v1.0.12). To establish if there were significant differences in specific gene list ranks between the samples, the Wilcoxon signed-rank test (two-sided) was used in pairwise comparisons.

Generation of hESC-AMs

NKX2.5eGFP/+-COUP-TFIImCherry/+ hESCs, as described before (35), were maintained as undifferentiated colonies in Essential 8 medium (Thermo Fisher Scientific, A1517001) on vitronectin (Thermo Fisher Scientific, A14700)-coated culture plastics. Differentiation of these cells to AMs was performed using the previously described spin embryoid body protocol with retinoic acid treatment (35,41). To generate pure populations of hESC-AMs, eGFP- and mCherry-double positive cells were purified around day 17 of differentiation using a Sony Biotechnology SH800 flow cytometer after exclusion of dead cells and debris according to side and forward scatter. After sorting, cells were suspended in TID medium (61) and transferred to vitronectin-coated 48-well culture plates to establish confluent monolayers. Optical voltage mapping of hESC-AMs was performed 5-11 days after replating.

Cellular electrophysiology

Differentiated hiAMs were dissociated by incubation with a 5 U/mL papain (Worthington Biochemical, LS003127) and 1 mM L-cysteine (Sigma-Aldrich, C6852) solution in PBS for 10 min at 37°C. Next, an equal volume of stop solution was added, consisting of 1 mg/mL soybean trypsin inhibitor (Sigma-Aldrich, T9253) and 40 µg/mL DNase I in PBS. Cells were pelleted by centrifugation for 5 min at 160×*g* at RT and plated at densities of 3-6×10^4 cells/cm^2 on fibronectin-coated 12-mm diameter glass coverslips (VWR International, 631-1577), and measured over the 3 following days.

Single-cell APs and membrane currents were recorded using Axopatch 200B and MultiClamp 700B amplifiers (Molecular Devices). Signals were low-pass filtered at 5-kHz cut-off frequency and digitized at 40 and 20 kHz for APs and membrane currents, respectively. Data acquisition and analysis were accomplished with pClamp (v10.7, Molecular Devices) and custom-made software. Series resistance was compensated by ≥ 80%. Patch pipettes were pulled from borosilicate glass (Harvard apparatus) and had resistances of 2.0-3.0 MΩ after filling with the solutions as indicated. Potentials were corrected for the calculated liquid junction potential (63). Cell membrane capacitance (C_m) was estimated by dividing the time constant of the decay of the capacitive transient in response to 5 mV hyperpolarizing voltage clamp steps from −40 mV by the series resistance.

APs were recorded using the amphotericin-perforated patch-clamp technique at 36 ± 0.2°C. The bath solution was a modified Tyrode's solution containing (in mM): 140 NaCl, 5.4 KCl, 1.8 $CaCl_2$, 1.0 $MgCl_2$, 5.5 glucose and 5.0 HEPES-NaOH (pH 7.4). The pipette solution contained (in mM): 125 K-gluconate, 20 KCl, 5.0 NaCl, 0.44 amphotericin B (Sigma-Aldrich, A2411) and 10 HEPES-KOH (pH 7.2). APs were elicited at 1-Hz by 3-ms, ~1.2× threshold current pulses through the patch pipette. Parameters from ten consecutive APs were averaged. APs from haAMs were measured in non-depolarized single, rod-shaped cardiomyocytes (64), which were isolated for a previous study (65). In short, cells were enzymatically isolated with the chunk method from left atrial appendages as described previously (65). These appendages were obtained from patients in sinus rhythm undergoing cardiac surgery (coronary bypass grafting or valve surgery), and included in the multicentre PREDICT AF study (66). The patient characteristics are as reported previously (65). Details on the Na^+ and K^+ current recordings in hiAMs are provided in the **Supplemental Methods**.

Optical voltage mapping

To assess AP properties and propagation in monolayers, hiAMs were seeded in fibronectin-coated 48-well, 24-well or 6-well culture plates at a density of 4×10^5 cells/cm^2 and differentiated as described. Alternatively, hESC-AMs were seeded at a density of 5.8×10^5 cells/cm^2 in vitronectin-coated 48-well culture plates. Cell layers of hiAMs or hESC-AMs were incubated with 8 µM di-4-ANEPPS (Thermo Fisher Scientific, D1119) in DMEM/F-12 (Thermo Fisher Scientific, 11039) for 10 min in a humidified 95% air-5% CO2 incubator at 37°C. Following incubation, medium was changed to fresh DMEM/F-12 and cells were placed on a 37°C warming plate for the duration of the experiment. During optical voltage mapping, excitation light (525 ± 25 nm) was delivered by a halogen arc-lamp through epi-illumination. Emission light passed through a dichroic mirror and a long-pass emission filter (> 590 nm). Signals were acquired using a 100×100 pixels complementary metal oxide semiconductor camera (MiCAM05-Ultima, SciMedia) at a spatial resolution of 165 (48/24-well) or 250 (6-well) µm/pixel, and a temporal resolution between 2 and 6 ms per frame depending on the type and duration of experiment. Acquisition times varied between 4 and 12 s for characterization studies, and up to 2 min for arrhythmia studies. Data was analysed using BrainVision Analyzer (v16.04.20, BrainVision). Signals were averaged with those of the 8 nearest neighbouring pixels to minimize noise artefacts. CV, APD and activation frequency were determined at a minimum of 5 different vectors/locations equally distributed throughout the culture. Arrhythmia wavelength was calculated by multiplying average CV and APD_{90}. Temporal excitation gap was calculated by subtracting APD_{90} during arrhythmic activation from the cycle length. Activation frequency over time was determined by analysing peak to peak intervals through a custom MATLAB (vR2016a, MathWorks) script on high-pass filtered data at selected locations in the culture.

Electrical stimulation and arrhythmia induction

Electrical point stimulation during optical voltage mapping was performed using an epoxy-coated bipolar platinum electrode, delivering 8-V, 10-ms square pulses. The electrode was connected to a STG 2004 stimulus generator (Multi Channel Systems) driven by MC Stimulus II software (v3.5.0, Multi Channel Systems). Baseline AP properties and propagation were calculated during 1-Hz electrical pacing (i.e. 1000-ms cycle length). Restitution was calculated by pacing at a cycle length of 1000 ms (S1) followed by an additional stimulus (S2) at a variable cycle length. Arrhythmia induction was performed by delivering 20 to 40 stimuli at the shortest cycle length at which 1:1 capture was maintained (range 90-180 ms), generally starting with a cycle length equal to the APD_{80}.

Arrhythmia studies and drug interventions

To determine relevant compound dosage, flecainide acetate salt (Sigma-Aldrich, F6777) dissolved in DMSO (CryoMACS, Miltenyi Biotec, 170-076-303), sotalol hydrochloride (Sigma-Aldrich, S0278) dissolved in demineralized water and DMSO (solvent/vehicle control), were tested on 2-cm^2 hiAM layers at increasing doses during optical voltage mapping, until loss of excitability. For each compound, 3 escalating doses were chosen, to include various effect sizes in a clinically relevant range. Induced reentrant circuits were monitored for 5 min to confirm stability before compounds were infused to study their effect on reentrant circuit characteristics. Flecainide, sotalol or DMSO as control, all at 3 concentrations, were slowly infused in a 1:1 volume ratio into cultures with reentrant circuits during optical voltage mapping using an infusion pump (Acromed Medical Systems) controlling infusion rate and volume (3 mL at 0.16 mL/s). Cultures were continuously monitored from 2 min prior to drug infusion until 10 min after the start of the drug treatment.

Cryopreservation

hiAMs at day 8 of cardiomyogenic differentiation were dissociated by papain treatment, pelleted by centrifugation and resuspended in cold (4°C) culture medium. Next, an equal volume of ice-cold 80% FBS/20% DMSO was added dropwise to the suspension, after which cryovials containing 10^6 cells/mL were frozen to –80°C at a rate of –1°C/min. Twenty-four h later, the cells were placed in nitrogen vapor for long-term storage. Cells were thawed by swirling vials in a 37°C bath, immediately followed by dropwise addition of cold (4°C) culture medium until a tenfold dilution was reached. Cells were pelleted by centrifugation, resuspended in supplemented hiAM differentiation medium and cultured for 6 days in this medium to complete differentiation. Cell viability after dissociation and after thawing as well as replating efficiency of the cells was determined by 0.4% Trypan Blue staining (1:1 ratio) and manual counting using a haemocytometer.

Statistics and Reproducibility

Statistical analyses were performed using GraphPad Prism (v8.0.1, GraphPad Software). Data are presented as mean ± standard deviation (SD) or mean ± standard error of the mean (SEM), unless otherwise indicated. Normally distributed data between independent groups was tested for statistical significance using the unpaired t-test (2 groups) or using the one-way analysis of variance with Tukey or Dunnett post-hoc analysis (3 or more groups). Dependent groups were tested using a paired t-test (2 groups) or using a repeated measure one-way analysis of variance with Tukey or Dunnett post-hoc analysis (3 or more groups). Non-normally distributed independent data were compared using the Mann-Whitney test. Dependent non-normally distributed data of multiple groups were compared using the Friedman test with Dunn post-hoc analysis. The stability of mean CV and APD at various PDs was tested by calculating the Pearson correlation coefficient. Rates of reentrant activity termination were compared between groups using the Chi-square test. All testing was performed two-sided. Statistical significance was expressed as following for clarity: *$P < 0.05$, **$P < 0.01$, ***$P < 0.001$. Precise *P*-values can be found in **Supplemental Data File 3**. Representative micrographs were chosen from a number of images (generally $n \geq 3$), based on multiple independent differentiations.

Data and materials availability

LV.iMHCK7.SV40-LT-WT particles can be obtained by academic research groups under a material transfer agreement (contact hiAM@lumc.nl for inquiries). The main data supporting the results in this study are available within the paper and its **Supplemental Information**. Certain raw and analysed datasets generated during the study are too large to be publicly shared, yet they are available for research purposes from the corresponding authors on reasonable request. The RNA-sequencing data described in this study is available at the NCBI's Gene Expression Omnibus (GEO) under GEO accession numbers GSE156824 and GSE178473. The Whole Genome Sequencing data is available under BioProject accession number PRJNA760786.

Acknowledgments

The authors thank Jia Liu (LUMC, Leiden, the Netherlands) for constructing plasmid pLV.iMHCK7.SV40-LT-WT and producing LV.iMHCK7.SV40-LT-WT particles, Tessa van Herwaarden (LUMC, Leiden, the Netherlands) for collecting human foetal atrial tissue, Bini Klein (LUMC, Leiden, the Netherlands) for donating the SV40 LT-encoding plasmid pAT153.SV40ori, Stephen Hauschka (University of Washington, Seattle, WA) for providing construct +aMHCKChCAT encoding the MHCK7 promoter, Didier Trono (Swiss Federal Institute of Technology Lausanne, Lausanne, Switzerland) for making available the LV shuttle plasmid pLVET-tTR-KRAB, Carolina Jost (LUMC, Leiden, the Netherlands) for assistance with interpretation and annotation of transmission electron microscopy data and Ursula Ravens (University of Freiburg, Freiburg, Germany) for useful discussions.

References

1. Robinson, N. B. et al. The current state of animal models in research: A review. *Int J Surg*. 2019;72:9-13.

2. Ruijtenberg, S. & van den Heuvel, S. Coordinating cell proliferation and differentiation: Antagonism between cell cycle regulators and cell type-specific gene expression. *Cell Cycle*. 2016;15:196-212.

3. Thomson, J. A. et al. Embryonic stem cell lines derived from human blastocysts. *Science*. 1998;282:1145-7.

4. Takahashi, K. et al. Induction of pluripotent stem cells from adult human fibroblasts by defined factors. *Cell*. 2007;131:861-72.

5. Yu, J. et al. Induced pluripotent stem cell lines derived from human somatic cells. *Science*. 2007;318:1917-20.

6. Kim, J., Koo, B. K. & Knoblich, J. A. Human organoids: model systems for human biology and medicine. *Nat Rev Mol Cell Biol*. 2020.

7. Liu, J. et al. Generation and primary characterization of iAM-1, a versatile new line of conditionally immortalized atrial myocytes with preserved cardiomyogenic differentiation capacity. *Cardiovasc Res*. 2018;114:1848-59.

8. Liu, J. et al. Conditionally immortalized brown preadipocytes can switch between proliferative and differentiated states. *Biochim Biophys Acta Mol Cell Biol Lipids*. 2019;1864:158511.

9. Deuschle, U., Meyer, W. K. & Thiesen, H. J. Tetracycline-reversible silencing of eukaryotic promoters. *Mol Cell Biol*. 1995;15:1907-14.

10. Szulc, J., Wiznerowicz, M., Sauvain, M. O., Trono, D. & Aebischer, P. A versatile tool for conditional gene expression and knockdown. *Nat Methods*. 2006;3:109-16.

11. Chugh, S. S. et al. Worldwide epidemiology of atrial fibrillation: a Global Burden of Disease 2010 Study. *Circulation*. 2014;129:837-47.

12. Kim, M. H., Johnston, S. S., Chu, B. C., Dalal, M. R. & Schulman, K. L. Estimation of total incremental health care costs in patients with atrial fibrillation in the United States. *Circ Cardiovasc Qual Outcomes*. 2011;4:313-20.

13. Nattel, S., Heijman, J., Zhou, L. & Dobrev, D. Molecular Basis of Atrial Fibrillation Pathophysiology and Therapy: A Translational Perspective. *Circ Res*. 2020;127:51-72.

14. Heijman, J., Guichard, J. B., Dobrev, D. & Nattel, S. Translational Challenges in Atrial Fibrillation. *Circ Res.* 2018;122:752-73.

15. Kirchhof, P. The future of atrial fibrillation management: integrated care and stratified therapy. *Lancet*. 2017;390:1873-87.

16. van Gorp, P. R. R., Trines, S. A., Pijnappels, D. A. & de Vries, A. A. F. Multicellular In vitro Models of Cardiac Arrhythmias: Focus on Atrial Fibrillation. *Front Cardiovasc Med*. 2020;7:43.

17. Salva, M. Z. et al. Design of tissue-specific regulatory cassettes for high-level rAAV-mediated expression in skeletal and cardiac muscle. *Mol Ther*. 2007;15:320-9.

18. Huttenbach, Y., Ostrowski, M. L., Thaller, D. & Kim, H. S. Cell proliferation in the growing human heart: MIB-1 immunostaining in preterm and term infants at autopsy. *Cardiovasc Pathol*. 2001;10:119-23.

19. Cui, Y. et al. Single-Cell Transcriptome Analysis Maps the Developmental Track of the Human Heart. *Cell Rep*. 2019;26:1934-50

20. Consortium, G. T. The Genotype-Tissue Expression (GTEx) project. *Nat Genet*. 2013;45:580-5.

21. Baker, M. Reproducibility: Respect your cells! *Nature*. 2016;537:433-5.

22. Narayan, S. M., Shivkumar, K., Krummen, D. E., Miller, J. M. & Rappel, W. J. Panoramic electrophysiological mapping but not electrogram morphology identifies stable sources for human atrial fibrillation: stable atrial fibrillation rotors and focal sources relate poorly to fractionated electrograms. *Circ Arrhythm Electrophysiol*. 2013;6:58-67.

23. Balouch, M. et al. Impact of rotor temperospatial stability on acute and one-year atrial fibrillation ablation outcomes. *Clin Cardiol*. 2017;40:383-9.

24. Laksman, Z. et al. Modeling Atrial Fibrillation using Human Embryonic Stem Cell-Derived Atrial Tissue. *Sci Rep*. 2017;7:5268.

25. Sanders, P. et al. Spectral analysis identifies sites of high-frequency activity maintaining atrial fibrillation in humans. *Circulation*. 2005;112:789-97.

26. Schuessler, R. B. et al. Spatial and temporal stability of the dominant frequency of activation in human atrial fibrillation. *J Electrocardiol*. 2006;39:S7-12.

27. Yoshida, K. et al. Left atrial pressure and dominant frequency of atrial fibrillation in humans. *Heart Rhythm*. 2011;8:181-7.

28. January, C. T. et al. 2014 AHA/ACC/HRS guideline for the management of patients with atrial fibrillation: a report of the American College of Cardiology/American Heart Association Task Force on Practice Guidelines and the Heart Rhythm Society. *J Am Coll Cardiol*. 2014;64:e1-76.

29. Kirchhof, P. et al. 2016 ESC Guidelines for the management of atrial fibrillation developed in collaboration with EACTS. *Eur Heart J*. 2016;37:2893-962.

30. Hindricks, G. et al. 2020 ESC Guidelines for the diagnosis and management of atrial fibrillation developed in collaboration with the European Association of Cardio-Thoracic Surgery (EACTS). *Eur Heart J*. 2020.

31. Sanguinetti, M. C. & Jurkiewicz, N. K. Two components of cardiac delayed rectifier K+ current. Differential sensitivity to block by class III antiarrhythmic agents. *J Gen Physiol*. 1990;96:195-215.

32. Melgari, D., Zhang, Y., El Harchi, A., Dempsey, C. E. & Hancox, J. C. Molecular basis of hERG potassium channel blockade by the class Ic antiarrhythmic flecainide. *J Mol Cell Cardiol*. 2015;86:42-53.

33. Davidson, M. M. et al. Novel cell lines derived from adult human ventricular cardiomyocytes. *J Mol Cell Cardiol*. 2005;39:133-47.

34. Goldman, B. I., Amin, K. M., Kubo, H., Singhal, A. & Wurzel, J. Human myocardial cell lines generated with SV40 temperature-sensitive mutant tsA58. *In Vitro Cell Dev Biol Anim*. 2006;42:324-31.

35. Schwach, V. et al. A COUP-TFII Human Embryonic Stem Cell Reporter Line to Identify and Select Atrial Cardiomyocytes. *Stem Cell Reports*. 2017;9:1765-79.

36. Ban, K., Bae, S. & Yoon, Y. S. Current Strategies and Challenges for Purification of Cardiomyocytes Derived from Human Pluripotent Stem Cells. *Theranostics*. 2017;7:2067-77.

37. Lee, J. H., Protze, S. I., Laksman, Z., Backx, P. H. & Keller, G. M. Human Pluripotent Stem Cell-Derived Atrial and Ventricular Cardiomyocytes Develop from Distinct Mesoderm Populations. *Cell Stem Cell*. 2017;21:179-94.

38. Argenziano, M. et al. Electrophysiologic Characterization of Calcium Handling in Human Induced Pluripotent Stem Cell-Derived Atrial Cardiomyocytes. *Stem Cell Reports*. 2018;10:1867-78.

39. Branco, M. A. et al. Transcriptomic analysis of 3D Cardiac Differentiation of Human Induced Pluripotent Stem Cells Reveals Faster Cardiomyocyte Maturation Compared to 2D Culture. *Sci Rep*. 2019;9:9229.

40. Buikema, J. W. et al. Wnt Activation and Reduced Cell-Cell Contact Synergistically Induce Massive Expansion of Functional Human iPSC-Derived Cardiomyocytes. *Cell Stem Cell*. 2020;27:50-63.

41. Devalla, H. D. et al. Atrial-like cardiomyocytes from human pluripotent stem cells are a robust preclinical model for assessing atrial-selective pharmacology. *EMBO Mol Med*. 2015;7:394-410.

42. Voigt, N. et al. Enhanced sarcoplasmic reticulum Ca2+ leak and increased Na+-Ca2+ exchanger function underlie delayed afterdepolarizations in patients with chronic atrial fibrillation. *Circulation*. 2012;125:2059-70.

43. Voigt, N. et al. Cellular and molecular mechanisms of atrial arrhythmogenesis in patients with paroxysmal atrial fibrillation. *Circulation*. 2014;129:145-56.

44. Heijman, J. et al. Atrial Myocyte NLRP3/CaMKII Nexus Forms a Substrate for Post-Operative Atrial Fibrillation. *Circ Res*. 2020.

45. Nakanishi, H. et al. Geometrical Patterning and Constituent Cell Heterogeneity Facilitate Electrical Conduction Disturbances in a Human Induced Pluripotent Stem Cell-Based Platform: An In vitro Disease Model of Atrial Arrhythmias. *Front Physiol*. 2019;10:818.

46. Goldfracht, I. et al. Generating ring-shaped engineered heart tissues from ventricular and atrial human pluripotent stem cell-derived cardiomyocytes. *Nat Commun*. 2020;11:75.

47. Harrild, D. & Henriquez, C. A computer model of normal conduction in the human atria. *Circ Res*. 2000;87:E25-36.

48. Valderrabano, M. Influence of anisotropic conduction properties in the propagation of the cardiac action potential. *Prog Biophys Mol Biol*. 2007;94:144-68/

49. Salvage, S. C. et al. Multiple targets for flecainide action: implications for cardiac arrhythmogenesis. *Br J Pharmacol*. 2018;175:1260-78.

50. Lemme, M. et al. Atrial-like Engineered Heart Tissue: An In Vitro Model of the Human Atrium. *Stem Cell Reports*. 2018;11:1378-90.

51. Zhao, Y. et al. A Platform for Generation of Chamber-Specific Cardiac Tissues and Disease Modeling. *Cell*. 2019;176:913-27.

52. Lee, A. et al. 3D bioprinting of collagen to rebuild components of the human heart. *Science*. 2019;365:482-7.

53. Yu, H. & Wang, Z. Cardiomyocyte-Derived Exosomes: Biological Functions and Potential Therapeutic Implications. *Front Physiol*. 2019;10:1049.

54. Chang, T. H., Ray, F. A., Thompson, D. A. & Schlegel, R. Disregulation of mitotic checkpoints and regulatory proteins following acute expression of SV40 large T antigen in diploid human cells. *Oncogene*. 1997;14:2383-93

55. Goette, A. et al. EHRA/HRS/APHRS/SOLAECE expert consensus on atrial cardiomyopathies: Definition, characterization, and clinical implication. *Heart Rhythm*. 2017;14:e3-e40.

56. DuBridge, R. B. et al. Analysis of mutation in human cells by using an Epstein-Barr virus shuttle system. *Mol Cell Biol*. 1987;7:379-87.

57. Chen, S., Zhou, Y., Chen, Y. & Gu, J. fastp: an ultra-fast all-in-one FASTQ preprocessor. *Bioinformatics*. 2018;34:i884-i90.

58. Patro, R., Duggal, G., Love, M. I., Irizarry, R. A. & Kingsford, C. Salmon provides fast and bias-aware quantification of transcript expression. *Nat Methods*. 2017;14:417-9.

59. Love, M. I. et al. Tximeta: Reference sequence checksums for provenance identification in RNA-seq. *PLoS Comput Biol*. 2020;16:e1007664.

60. Stuart, T. et al. Comprehensive Integration of Single-Cell Data. *Cell*. 2019;177:1888-902.

61. Love, M. I., Huber, W. & Anders, S. Moderated estimation of fold change and dispersion for RNA-seq data with DESeq2. *Genome Biol*. 2014;15:550.

62. Birket, M. J. et al. Contractile Defect Caused by Mutation in MYBPC3 Revealed under Conditions Optimized for Human PSC-Cardiomyocyte Function. *Cell Rep*. 2015;13:733-45.

63. Barry, P. H. & Lynch, J. W. Liquid junction potentials and small cell effects in patch-clamp analysis. *J Membr Biol*. 1991;121:101-17.

64. Verkerk, A. O. et al. Patch-Clamp Recordings of Action Potentials From Human Atrial Myocytes: Optimization Through Dynamic Clamp. *Front Pharmacol*. 2021;12:649414.

65. Casini, S. et al. Absence of Functional Nav1.8 Channels in Non-diseased Atrial and Ventricular Cardiomyocytes. *Cardiovasc Drugs Ther*. 2019;33:649-60.

66. van den Berg, N. W. E. et al. PREventive left atrial appenDage resection for the predICtion of fuTure atrial fibrillation: design of the PREDICT AF study. *J Cardiovasc Med (Hagerstown)*. 2019;20:752-61.

Supplemental Methods

Flow cytometric assessment of human immortalized atrial myocyte (hiAM) ploidy

For assessment of ploidy, differentiated hiAMs were detached using papain, pelleted by centrifugation (200×*g*, 5 min) and fixed by a 20-min incubation with 90% methanol of -20°C. Prior to fixation, half of the cell suspension was spiked with peripheral blood mononuclear cells (PBMCs) to provide a diploid standard. Following the addition of an equal volume of ice-cold PBS-0.1% TWEEN 20 (PBST; Sigma-Aldrich, P1379), the cells were pelleted, washed with ice-cold PBST, stained with 2.5 μM DAPI (BioLegend, 422801) in PBS/5.0% bovine serum albumin (BSA)/0.5% TWEEN 20 by incubation for 30 min at room temperature (RT) and stored overnight at 4°C in the same solution before measurement. Prior to flow cytometric analysis on the FACSCanto II with FACSDiva 8.0 software (both from BD Biosciences), samples were filtered through a cell strainer with a 35-μm nylon mesh (Falcon Tube with Filter Cap, Thermo Fisher Scientific, 352235). Cytometer Setup and Tracking beads (BD Biosciences, 641319) were used to check cytometer performance and guaranty data quality. Cells were excited using solid state lasers of 20 mW and 488 nm and of 60 mW and 405 nm. Forward scatter (FSC), side scatter (SSC) and DAPI fluorescence (452/45 nm band pass filter) area (A), height (H) and width (W) were recorded and stored as FCS 3.0 list mode data files. During acquisition a live gate was applied selecting single-cell events using DAPI-A vs DAPI-W pulse processing. A minimum of 30,000 single-cell events were collected of each sample using a low flow rate, maintaining optimal hydrodynamic focusing. Data were analysed using WinList 8 linked to ModFit LT 5.0 (both from Verity Software House) using 256 channel resolution for DNA content analysis. The relative median channel number of the PBMCs' G1 population was used as DNA diploid reference to determine hiAM ploidy. A hypodiploid, aneuploid 2, aneuploid 3 statistical model was used for analysis, as this provided the best fit (*i.e.* fair to good) with a reduced Chi-square (RCS) never exceeding 3.2. Additionally, ModFit LT handled aggregates and debris after manual correction for evident aggregates using DAPI-A vs DAPI-W pulse processing.

Flow cytometric assessment of hiAM purity

Differentiated hiAMs were detached using papain, pelleted by centrifugation (200×*g*, 5 min), fixed by incubation with 4% buffered formaldehyde for 15 min at RT and permeabilized by a treatment of ≥ 20 min with 90% methanol of -

20°C. hiAMs were incubated with primary antibodies in PBS-0.5% BSA for 1 h at RT followed by a 30-min incubation at RT with Alexa 488-conjugated secondary antibodies in PBS-0.5% BSA. Between each step, cells were washed twice with PBS-0.5% BSA. For an overview of the antibodies and the dilutions at which they were used, see **Supplemental Table 5**. Analysis was performed with an Accuri C6 flow cytometer (BD Biosciences), equipped with 473- and 552-nm lasers. The hiAM samples were excited with the 473-nm laser and the emitted light was passed through a 586/15 nm band pass filter before being captured by the photodetector. Cells stained only with the fluorochrome-conjugated secondary antibody were included as control. Gating of hiAMs was performed as shown in **Supplemental Figure 4**. Per sample, 5,000-20,000 gated events were analysed using the BD Accuri C6 Software (v1.0.264).

Transmission electron microscopy

Differentiated hiAMs were fixed for 1 h at RT by addition of an equal volume of fixative (3% glutaraldehyde in 0.1 M cacodylate buffer pH 7.4) to the hiAM culture medium. After washing the monolayers 3 times with 0.1 M cacodylate buffer, the cells were post-fixed for 1 h on ice with 1% osmium tetroxide, 1.5% potassium ferricyanide in 0.1 M cacodylate buffer. Next, the sample was dehydrated by a graded series of ethanol in water followed by a graded series of LX 112 resin (Ladd Research, 21210) in ethanol. After the final incubation step with 100% LX 112, BEEM capsules (Tedd Pella, 21600) filled with LX 112 were placed on the fixed cells. After polymerization of the LX 112, the BEEM capsules were snapped off the surface of the culture dishes. Ultrathin sections (90 nm) parallel to the surface were made on a Reichert Ultracut S (Leica Microsystems). Following post-staining of the sections with uranyl acetate and lead citrate, the electron microscopy images were taken with a FEI Technai Twin T12 transmission electron microscope (Thermo Fisher Scientific) operating at 120 kV, using a Gatan OneView camera on binning 2. Overlapping images were collected and stitched together into a big image as described (67).

TBX5 knockdown

Oligodeoxyribonucleotides for generating a lentiviral vector (LV) encoding a short hairpin RNA (shRNA) targeting all transcripts of human TBX5 were designed with the aid of the GPP Web Portal from the Broad Institute. To rule out off-target effects, a target sequence was selected that did not show an overlap of > 13 nucleotides with any other human transcript as determined using BlastN (National Center for Biotechnology Information). The sequences of the oligodeoxyribonucleotides for generating a control shRNA targeting firefly luciferase (PpLuc) were derived from the MISSION shRNA Library (SHC007, Sigma-Aldrich). The annealing products of both oligodeoxyribonucleotide pairs (see **Supplemental Table 6** for nucleotide sequences) were inserted in between the human RNU6-1 gene promoter and an RNA polymerase III termination sequence of an LV shuttle plasmid that also contained a human UBC gene (HsUBC) promoter-driven expression unit encoding the Aequorea victoria enhanced green fluorescent protein (eGFP). The correctness of the shRNA-encoding constructs was validated by diagnostic restriction enzyme digestions as well as by Sanger sequencing. LV production was performed as described in the main manuscript.

Whole genome sequencing

Genomic DNA of 5×10^5 proliferating hiAMs was isolated using the ISOLATE II Genomic DNA Kit (Meridian Bioscience, BIO-52066) according to manufacturer's instructions. Samples were sent to BGI Genomics for whole genome sequencing. Here, following quality control by agarose gel electrophoresis, genomic DNA was fragmented by sonification (Covaris). Fragments with an average length of 350 base pairs were selected and underwent end-repairing and A-tailing reactions. Adapters were ligated to A-tailed fragments and amplified by ligation-mediated polymerase chain reaction. The amplified DNA fragments were then denatured and circularized by splint-mediated DNA ligation. After removal of remaining non-circularized DNA templates by exonuclease treatment, the single-stranded DNA circles were converted into DNA nanoballs (DNBs) by rolling circle amplification. The DNBs were loaded into patterned nanoarrays and pair-end sequencing was performed on the BGISEQ-500 platform. Sequencing-derived raw image files were processed by BGISEQ-500 base calling software. Raw data was filtered to remove reads containing sequencing adapters, reads whose low-quality base ratio (base quality ≤ 5) was more than 50% and reads whose unknown base ('N' base) ratio was more than 10%. These clean reads were aligned to human reference genome GRCh37 using Burrows-Wheeler Aligner (v0.7.12). Local realignment around insertions/deletions and base quality score recalibration were performed using GATK (v3.3.0), with duplicate reads removed by Picard (v1.118). Lentiviral integration sites were determined by locating reads that aligned to (one of the termini of) the proviral DNA sequence of LV.iMHCK7.LT-WT and to the human reference genome.

Ca^{2+} imaging

To compare Ca^{2+} handling of hiAMs and human embryonic stem cell-derived atrial cardiomyocytes (hESC-AMs), the same protocol was used as described in the main text for optical voltage mapping except that the cellular monolayers (all in 48-well format) were incubated with 2.5 μM RHOD-2 AM (Thermo Fisher Scientific, R1245MP) instead of di-4-ANEPPS in DMEM/F-12 for 30 min. The same imaging system and filter sets were used as for optical voltage mapping and data was recorded at a spatial resolution of 165 μm/pixel and a temporal resolution of 6 ms per frame. Data were analysed using BrainVision Analyzer software (Brain Products) and noise artefacts were minimized by averaging of the signals at a selected pixel and its 8 nearest neighbours. Signal amplitude of the Ca^{2+} transient, time to peak, 50% decay time and conduction velocity (CV) were determined at multiple locations equally distributed throughout the culture. The effect of L-type Ca^{2+} channel activity modulation on Ca^{2+} handling by hiAMs and hESC-AMs was studied using the antagonist verapamil hydrochloride (Sigma-Aldrich, V4629) and agonist Bay K8644 (Sigma-Aldrich, B112). Both drugs were added from 10 mM stock solutions in dimethylsulfoxide (DMSO) to the hiAM and hESC-AM layers.

Cellular electrophysiology extended

The Na^+ current (I_{Na}) was recorded using the ruptured whole cell configuration at RT (21 ± 0.2°C). The bath solution for I_{Na} recordings contained (in mM): NaCl 20, CsCl 120, $CaCl_2$ 1.8, $MgCl_2$ 1.0, glucose 5.5, HEPES 5.0, pH 7.4 (CsOH). Nifedipine (5 μM) was added to block the L-type Ca^{2+} current. Pipette solution contained (in mM): NaCl 3.0, CsCl 133, $MgCl_2$ 2.0, Na_2ATP 2.0, TEACl 2.0, EGTA 10, HEPES 5.0, pH 7.2 (CsOH). The current-voltage (I-V) relationship and voltage dependency of (in)activation were determined by means of custom voltage-clamp protocols as depicted schematically in **Supplemental Figure 12a,c**. In short, I_{Na} density and voltage dependence of activation were determined by 50-ms depolarizing pulses (between -80 and +40 mV) from a holding potential of –120 mV. Voltage-dependent inactivation was obtained by measuring the peak currents during a 50-ms test step to -20 mV, which followed a 500-ms prepulse to membrane potentials between -140 and -20 mV to allow inactivation. The holding potential was –120 mV. All voltage clamp steps were applied with a 5-sec cycle length. Peak I_{Na} was defined as the difference between peak and steady-state current. Current density was calculated by dividing the measured currents by cell capacitance (C_m). To determine the activation characteristics of I_{Na}, I-V curves were corrected for differences in driving force and normalized to maximum peak current. Steady-state activation and inactivation curves were fitted using the Boltzmann equation I/Imax=A/(1+exp((V1/2-V)/k)) to determine V1/2 (membrane potential for the half-maximal [in]activation) and the slope factor k. K^+ currents were recorded using the amphotericin-perforated patch-clamp technique at 36 ± 0.2°C with similar solutions as used for the action potential (AP) recordings. K^+ currents were determined by means of custom voltage-clamp protocols as depicted schematically in the **Supplemental Figure 12d,f,g**. K^+ currents were activated in response to 500-ms steps from different holding potentials (-40 and -80 mV) to voltages ranging from -120 to +50 mV in 10-mV increments. All voltage clamp steps were applied with a 5-sec cycle length. Steady-state K^+ currents were defined as the current at the end of the 500-ms voltage steps. Transient outward K^+ current was defined as the difference between the peak outward current and the current amplitude at the end of the 500-ms voltage clamp step. The ultrarapid component of the delayed rectifier K^+ current (I_{Kur}) was measured as the steady-state current sensitive to 50 μM 4 aminopyridine (4-AP, Sigma-Aldrich, A78403) (68,69). All currents were normalized for cell size by dividing current amplitude by C_m.

Immunocytochemistry imaging

The Eclipse 80i Upright Microscope (Nikon) was equipped with filter blocks (all from Nikon): C-FL EPI-FL DAPI (MBE41300, Excitation: 340-380 nm, Emission: 435-485 nm), C-FL EPI-FL TRITC (MBE45600, Excitation: 540/25 nm, Emission: 605/55 nm), C-FL EPI-FL FITC (MBE44720, Excitation: 465-495 nm, Emission: 515-555), and lenses: CFI Plan Fluor 20X (N20XW-PF, Nikon) and CFI Plan Fluor 40X (N40XW-PF, Nikon). Exposure times varied between 100-300ms, depending on the staining. Confocal images were acquired in 3 channels using the TCS SP8 White Light Laser Confocal Microscope (Leica Microsystems) with the following settings: Channel 1, Laser (405 nm) intensity 0.5-1%, HyD (410-499 nm) gain 30. Channel 2, Laser (499 nm) intensity 1-2%, HyD (505-607 nm) gain 30. Channel 3, Laser (577 nm) intensity 2-5%, HyD (607-757 nm) gain 30. Intensity depended on the staining. The images were acquired using the HC PL APO CS2 63x/1.40 OIL lens (11506350, Leica Microsystems). Averaging of 3 frames was applied. The scan speed was 600 Hz, pinhole 95.5 μm and Z-stacking up to 10 frames was applied (thickness 0.4-1 μm).

Supplemental Results

Ploidy of hiAMs

Assessment of hiAM ploidy was performed using differentiated hiAM-2.38, -2.52 and -2.90 at population doublings (PDs) 35-37. These PDs are in the middle of those used to generate the other data in this study for which cells from PD 28-46 were employed. The DNA content of the 3 clones was very similar showing small populations of cells with average DNA indexes (DIs) of 0.9 and 3.5, and a large population of cells with an average DI of 1.7. (**Supplemental Figure 2**). These 3 cell populations, comprised on average 6.9, 9.1 and 84.1% of all cells, respectively. Due to the technical difficulty to exclude all cell doublets from the analysis, some of the cells with an apparent DI of 3.5 may actually consists of cell pairs with a DI of 1.7. Data per clone can be found in **Supplemental Table 2**.

Ca2+ dynamics of hESC-AMs and hiAMs

Baseline comparison of optical Ca^{2+} transients revealed significantly longer time to peak durations, shorter 50% decay times and lower CVs in 1-cm^2 hESC-AM layers when compared to equally sized layers of differentiated hiAMs (**Supplemental Figure 14a-c**). Additionally, hESC-AMs and hiAMs responded differently to the L-type Ca^{2+} channel modulators verapamil and Bay K8644 (**Supplemental Figure 14d,e**). Most notably, the amplitude of Ca^{2+} transients in hESC-AMs was strongly reduced by 100 nM verapamil, while the same concentration of verapamil had only a minimal inhibitory effect on hiAMs. Furthermore, hESC-AMs did no longer exhibit any Ca^{2+} transients in the presence of 1 µM verapamil, whereas these were still observed in hiAMs. For reference, the therapeutic serum concentration of verapamil was reported to be 0.2-0.9 µM (70). Extreme sensitivity to L-type Ca^{2+} current blockade and subsequent loss of Ca^{2+} transients has been previously described in human pluripotent stem cell-derived cardiomyocytes (71), suggesting deficient Ca^{2+}-induced Ca^{2+} release as the most likely mechanism. Another interesting observation is the respective decrease and increase of CV in the presence of verapamil and Bay K8644 only seen in hESC-AM layers. Taken together with the significantly lower expression of SCN5A (Nav1.5) in hESC-AMs compared to hiAMs (**Supplemental Data File 2**), these data might suggest a larger dependence on an increase of cytosolic Ca^{2+} in the generation and propagation of APs in hESC-AM layers.

Effect of TBX5 knockdown on Ca^{2+} dynamics in hiAMs

Holt-Oram syndrome, which is characterized by developmental heart defects, diastolic dysfunction and arrhythmias, is caused by mutations in the TBX5 gene (72,73). Previous studies have indicated disrupted Ca^{2+} handling as important mechanism for the diastolic dysfunction reported in Holt-Oram patients (74). To test the suitability of hiAMs for disease modelling beyond atrial arrhythmias, we studied the effect of decreased TBX5 expression on Ca^{2+} dynamics. For this purpose, hiAM-2.52 layers were transduced shortly after initiation of differentiation with different doses of LVs encoding a TBX5-specific shRNA or a negative control PpLuc-specific shRNA. Following 12 days of differentiation, this resulted in a 2- to 8-fold decrease in TBX5 protein levels for the lowest and highest dose of the TBX5-specific shRNA-encoding vector when compared to unmodified hiAMs (**Supplemental Figure 21a,b**). Subsequent optical Ca^{2+} imaging revealed dose-dependent changes in Ca^{2+} transients after TBX5 knockdown compared to control hiAMs (**Supplemental Figure 21c,d**). Specifically, TBX5 knockdown resulted in significantly lower Ca^{2+} signal amplitudes, longer time to peak durations and slower CVs. As expected, no changes in Ca^{2+} transients were observed following PpLuc knockdown. These findings confirm the results of previous studies in which a reduction in TBX5 expression in cardiomyocytes caused disturbances of normal Ca^{2+} handling in these cells (75-77). Overall, these data demonstrate that genetic modification of hiAMs is straightforward and illustrate their suitability for human disease studies beyond atrial arrhythmia modelling.

Supplemental Discussion

Conditional immortalization of human cardiomyocytes using simian virus 40 (SV40) large T (LT)

In the past, SV40 LT has been successfully used to generate lines of various types of foetal, neonatal and adult parenchymal human cells with phenotypic properties resembling those of the primary cells from which they were derived (78-80). Several of these cell lines have found widespread use 1) for fundamental research, 2) as models of human disease and for 3) pharmacological and toxicological screening. Davidson and colleagues (81) showed that SV40 LT is also able to immortalize ventricular cardiomyocytes of human adults (haVMs) but the resulting AC16 cells were not excitable and not contractile. The most likely explanation for the loss of cardiomyocyte functionality in the AC16 cells is the specific technique used to generate these cells, which involved the fusion of SV40 LT-transformed human skin fibroblasts with haVMs. The permanent expression of LT in these cells together with the (initial) presence of two nuclei executing distinct gene expression programs may have resulted in loss of their cardiomyocyte identity. This idea is supported by our observation that continuous expression of LT blocks the differentiation of hiAMs into functional cardiomyocytes (**Supplemental Figure 8**). An advantage of the approach used by Davidson et al. is that the cardiomyocytes are exposed to high levels of LT immediately after cell fusion allowing their rapid conversion into proliferative cells. In contrast, after transduction with LV.iMHCK7.LT-WT particles, it takes several days before cardiomyocytes produce substantial amount of LT. Thus, the main challenge for the successful application of our condition cell immortalization system to adult human cardiomyocytes seems to be to keep the cells in a proper condition long enough to enter into a proliferative state.

Supplemental References

67. Faas, F. G. et al. Virtual nanoscopy: generation of ultra-large high resolution electron microscopy maps. J Cell Biol. 2012;198:457-469.

68. Wang, Z., Fermini, B. & Nattel, S. Sustained depolarization-induced outward current in human atrial myocytes. Evidence for a novel delayed rectifier K+ current similar to Kv1.5 cloned channel currents. Circ Res. 1993;73:1061-1076.

69. Caballero, R. et al. In humans, chronic atrial fibrillation decreases the transient outward current and ultrarapid component of the delayed rectifier current differentially on each atria and increases the slow component of the delayed rectifier current in both. J Am Coll Cardiol. 2010;55:2346-2354.

70. Opie, L. H. Pharmacological differences between calcium antagonists. Eur Heart J. 1997;18 Suppl A:A71-79.

71. Itzhaki, I. et al. Calcium handling in human induced pluripotent stem cell derived cardiomyocytes. PLoS One. 2011;6:e18037.

72. Basson, C. T. et al. Mutations in human TBX5 [corrected] cause limb and cardiac malformation in Holt-Oram syndrome. Nat Genet. 1997;15:30-35.

73. Li, Q. Y. et al. Holt-Oram syndrome is caused by mutations in TBX5, a member of the Brachyury (T) gene family. Nat Genet. 1997;15:21-29.

74. Zhu, Y. et al. Tbx5-dependent pathway regulating diastolic function in congenital heart disease. Proc Natl Acad Sci U S A. 2008;105:5519-5524.

75. Nadadur, R. D. et al. Pitx2 modulates a Tbx5-dependent gene regulatory network to maintain atrial rhythm. Sci Transl Med. 2016;8:354ra115.

76. Churko, J. M. et al. Defining human cardiac transcription factor hierarchies using integrated single-cell heterogeneity analysis. Nat Commun. 2018;9:4906.

77. Kathiriya, I. S. et al. Modeling Human TBX5 Haploinsufficiency Predicts Regulatory Networks for Congenital Heart Disease. Dev Cell. 2021;56:292-309.

78. Ramboer, E. et al. Strategies for immortalization of primary hepatocytes. J Hepatol. 2014;61:925-943.

79. Scharfmann, R., Staels, W. & Albagli, O. The supply chain of human pancreatic beta cell lines. J Clin Invest. 2019;129:3511-3520.

80. Sato, M., Shay, J. W. & Minna, J. D. Immortalized normal human lung epithelial cell models for studying lung cancer biology. Respir Investig. 2020;58:344-354.

81. Davidson, M. M. et al. Novel cell lines derived from adult human ventricular cardiomyocytes. J Mol Cell Cardiol. 2005;39:133-147.

Supplemental Data

Supplemental Figure 1 (legend on next page).

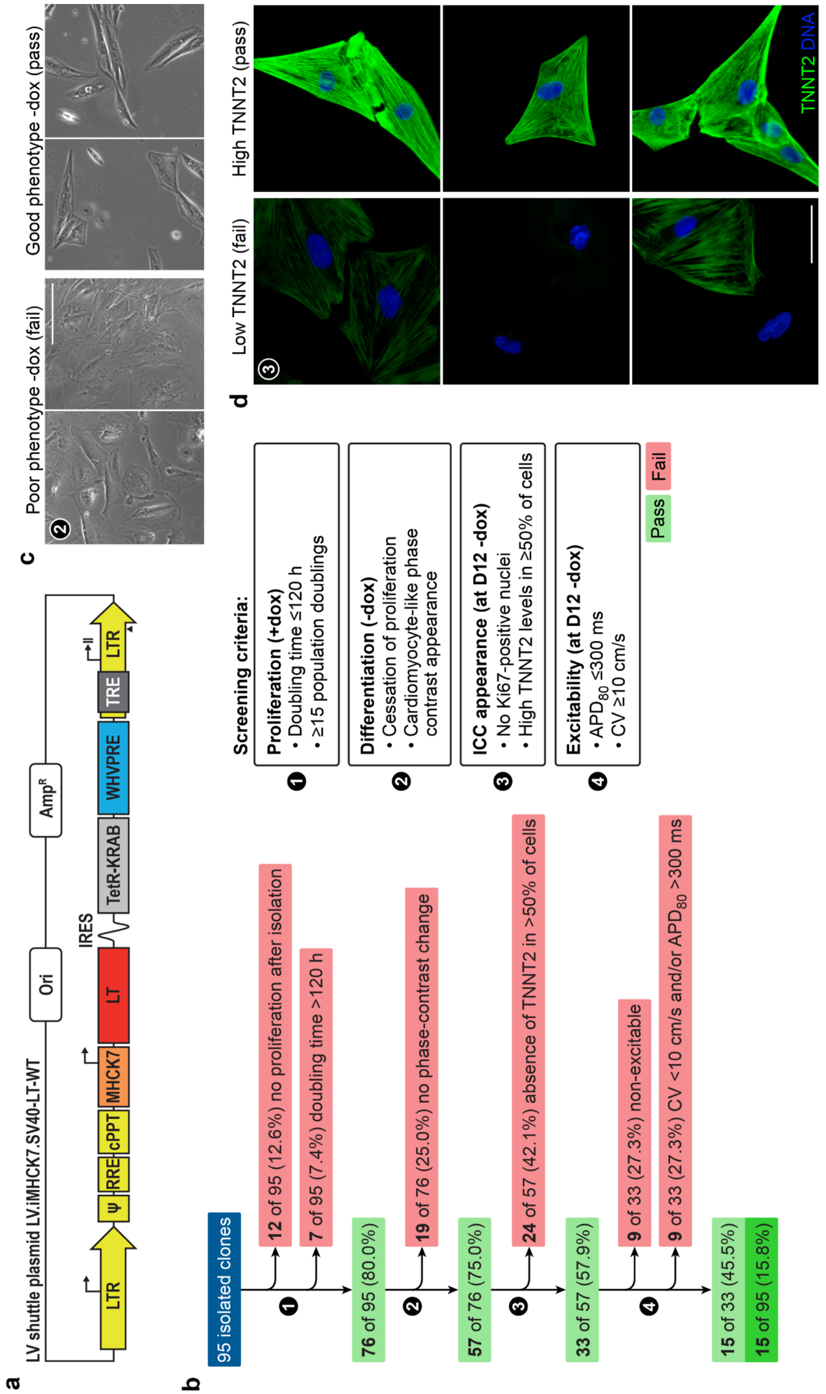

Supplemental Figure 1 (previous page). Extended data on the generation and selection of hiAM monoclones. **(a)** LV shuttle plasmid LV.iMHCK7.SV40-LT-WT. Ori, bacterial origin of replication. Amp^R, *Escherichia coli* ß-lactamase gene. LTR, human immunodeficiency virus type 1 (HIV1) long terminal repeat. ψ, HIV1 packaging signal. RRE, HIV1 Rev-responsive element. cPPT, HIV1 central polypurine tract and termination site. MHCK7, chimeric striated muscle-specific promoter. LT, coding sequence of wildtype oncogenic SV40 LT antigen. IRES, encephalomyocarditis virus internal ribosome entry site. TetR-KRAB, coding sequence of hybrid tetracycline-controlled transcriptional repressor. WHVPRE, woodchuck hepatitis virus posttranscriptional regulatory element. TRE, tetracycline-responsive promoter element consisting of 7 repeats of a 19-nucleotide tetracycline operator (tetO) sequence. **(b)** Extended flowchart of hiAM clone selection based on 4 main criteria with corresponding drop-off rates. ICC, Immunocytochemistry. TNNT2, cardiac troponin T. **(c)** Example of 2 hiAM monoclones displaying no cardiomyocyte-like change in phase contrast and of 2 monoclones showing a cardiomyocyte-like alteration in phase contrast after 12 days of culture in the absence of doxycycline (dox; criterion 2, differentiation). Scale bar, 100 µm. **(d)** Example of 3 hiAM monoclones that do and of 3 hiAM clones that do not pass the third criterion (*i.e.* immunocytochemical appearance) due to high and low TNNT2 expression, respectively, as assessed by ICC. Scale bar, 50 µm.

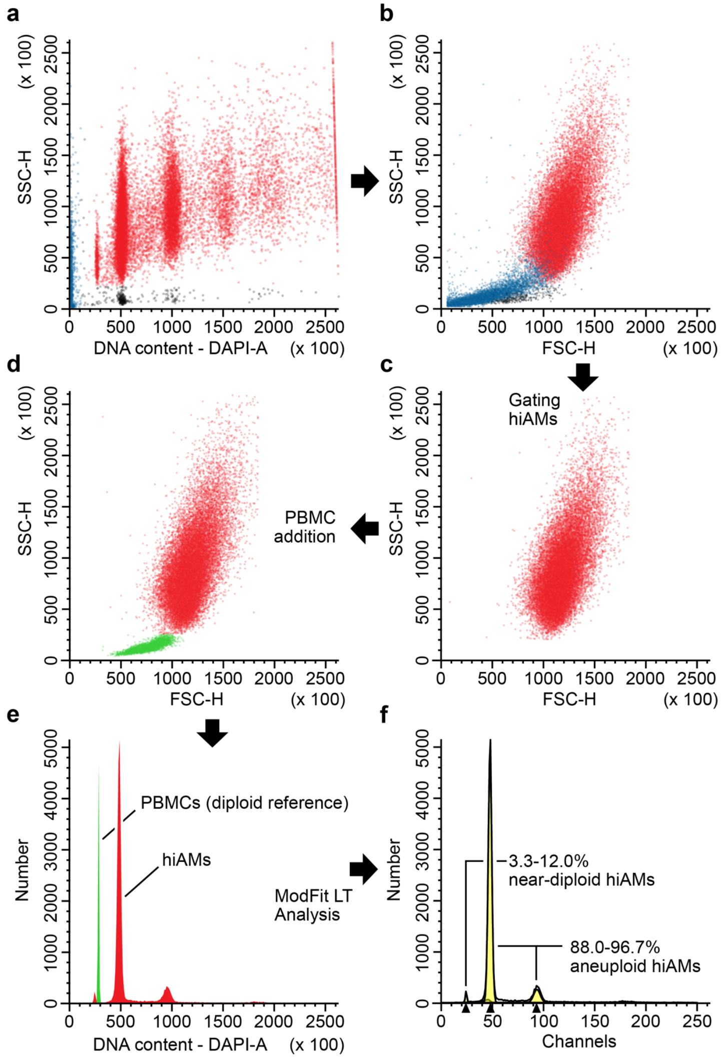

Supplemental Figure 2. Flow cytometric assessment of hiAM ploidy. Diagram showing the process of determining the ploidy of differentiated hiAMs with female peripheral blood mononuclear cells (PBMCs) serving as diploid reference. Scatter plots of **(a)** side scatter height (SSC-H) *vs.* DAPI fluorescence area (DAPI-A) and **(b)** SSC-H *vs.* forward scatter height (FSC-H) showing all events (red: hiAMs, blue: debris, black: bare nuclei). **(c)** Plot of the hiAMs gated based on the SSC-H *vs.* DAPI-A scatter plot and **(d)** discrimination of added PBMCs (green) based on their significant lower FSC-H and SSC-H signals compared to hiAMs. **(e)** DNA histogram of the PBMC/hiAM mixture after removal of evident aggregates. **(f)** Representative graph of the ModFit LT analysis revealing the different hiAM populations.

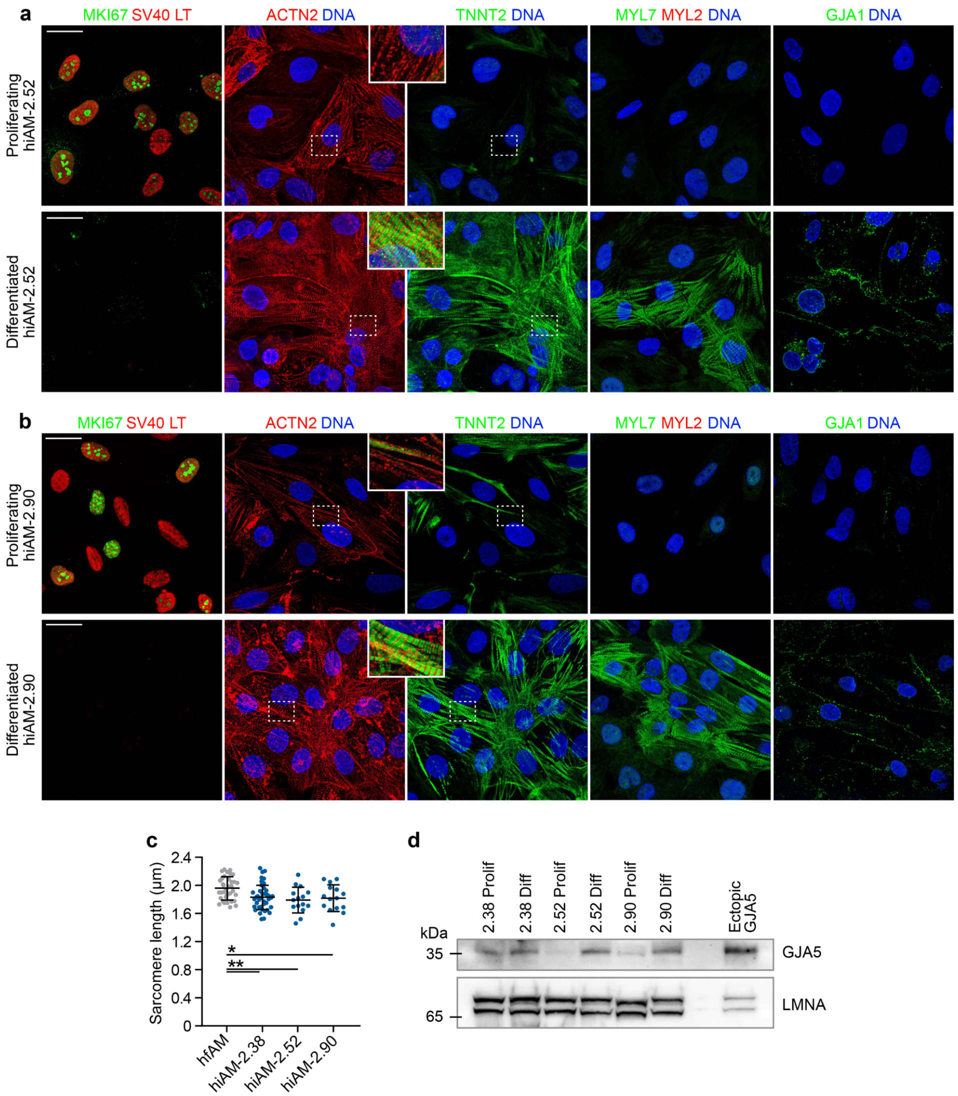

Supplemental Figure 3. Extended characterization of the hiAM phenotype during proliferation and after 12 days of differentiation. Proliferating and differentiated **(a)** hiAM-2.52 and **(b)** hiAM-2.90 were immunostained for Ki-67 (MKI67), SV40 LT, α-actinin 2 (ACTN2), cardiac muscle troponin T (TNNT2), the atrial and ventricular isoform of myosin regulatory light chain 2 (MYL7 and MYL2, respectively) and connexin 43 (GJA1). Scale bar, 25 µm. **(c)** Sarcomere length of hfAMs (*n* = 42 measurements from 14 images), hiAM-2.38 (*n* = 45 measurements from 15 images), hiAM-2.52 (*n* = measurements 15 from 5 images) and hiAM-2.90 (*n* = measurements 15 from 5 images) calculated based on z-line distance in cell layers stained for ACTN2. Mean shown, with error bars indicating standard deviation [SD]. **P* < 0.05, ***P* < 0.01, one-way analysis of variance with Tukey *post-hoc* analysis. **(d)** Connexin 40 (GJA5) protein levels of hiAM-

2.38, -2.52 and -2.90 during proliferation (Prolif) and after differentiation (Diff). Lamin A/C (LMNA) is included as loading control. Ectopically expressed connexin 40 is included as positive/size control. See **Supplemental File 4** for uncropped blots.

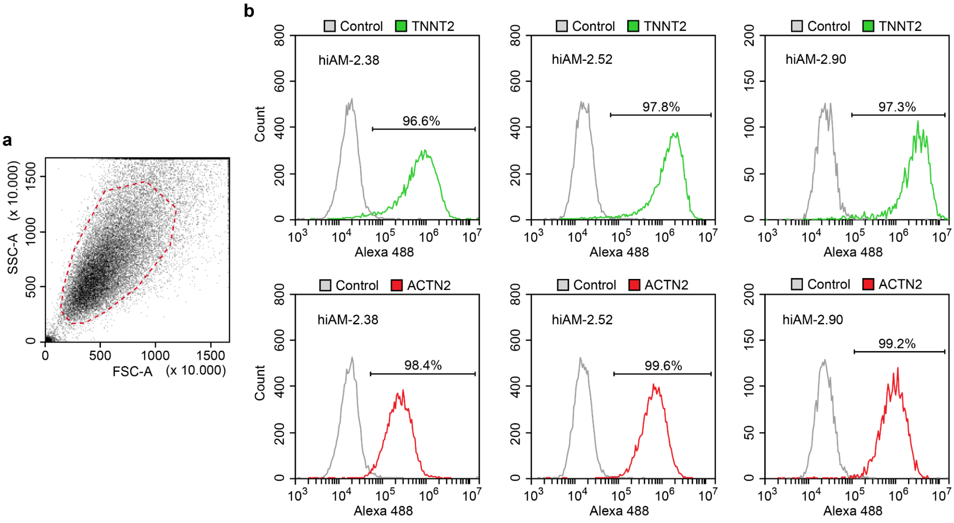

Supplemental Figure 4. Flow cytometric assessment of differentiated hiAM purity. **(a)** Representative side scatter area (SSC-A) *vs.* forward scatter area (FSC-A) plot showing all events. The red dotted line demarcates the hiAM population used for quantification. **(b)** Quantification of the proportion of differentiated hiAM-2.38, -2.52 and -2.90 staining positive for cardiac muscle troponin T (TNNT2) or α-actinin 2 (ACTN2).

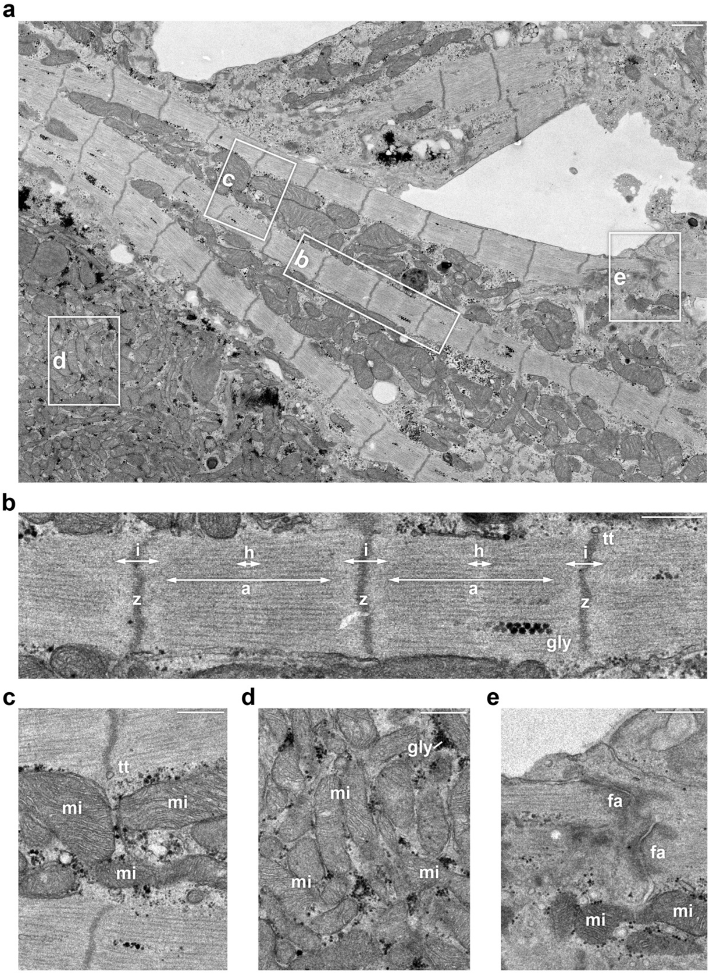

Supplemental Figure 5. Ultrastructural properties of differentiated hiAMs. **(a)** Transmission electron microscope image of differentiated hiAM-2.52. **(b)** Detailed view of sarcomeric organization (a, a-band. h, h-zone. i, i-band. z, z-line. gly, glycogen granules). The average sarcomere distance measured in overview **(a)** was 1.80 ± 0.11 µm. T-tubule-like structures (tt) were observed at the z-lines. **(c)** Mitochondria (mi) in between myofibrils. **(d)** Large cluster of perinuclear mitochondria and glycogen granules. **(e)** Intercalated disc connecting neighbouring hiAMs. fa, fascia adherens. **(a)** Scale bar, 1 µm. **(b-e)** Scale bar, 500 nm.

Supplemental Figure 6 (next page). Extended data on gene set enrichment analysis. Enriched GO terms (*P*-adjusted < 0.05) in proliferating hiAMs (left, red) and in differentiated hiAMs (blue, right).

Supplemental Figure 6
(legend on previous page)

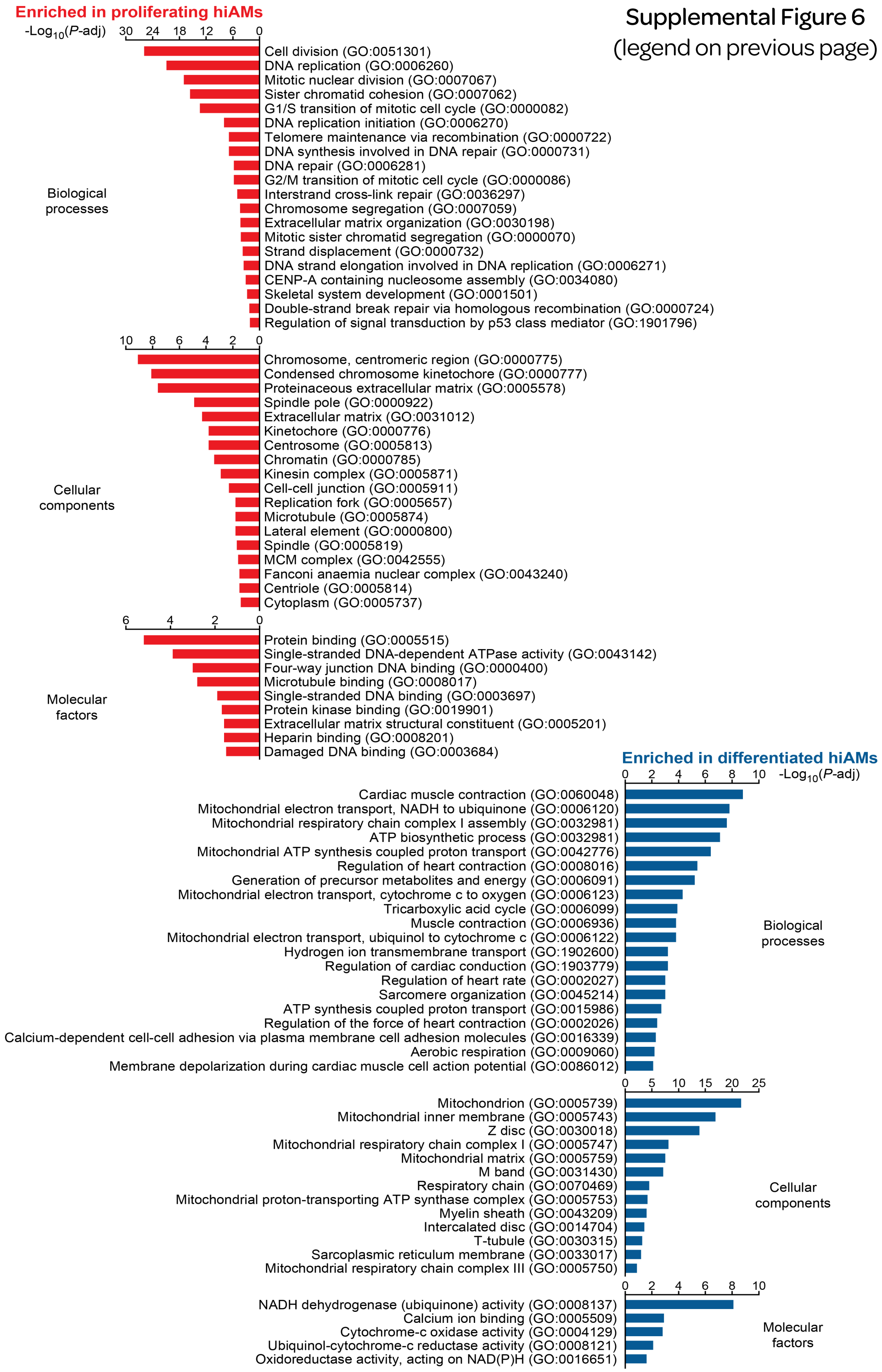

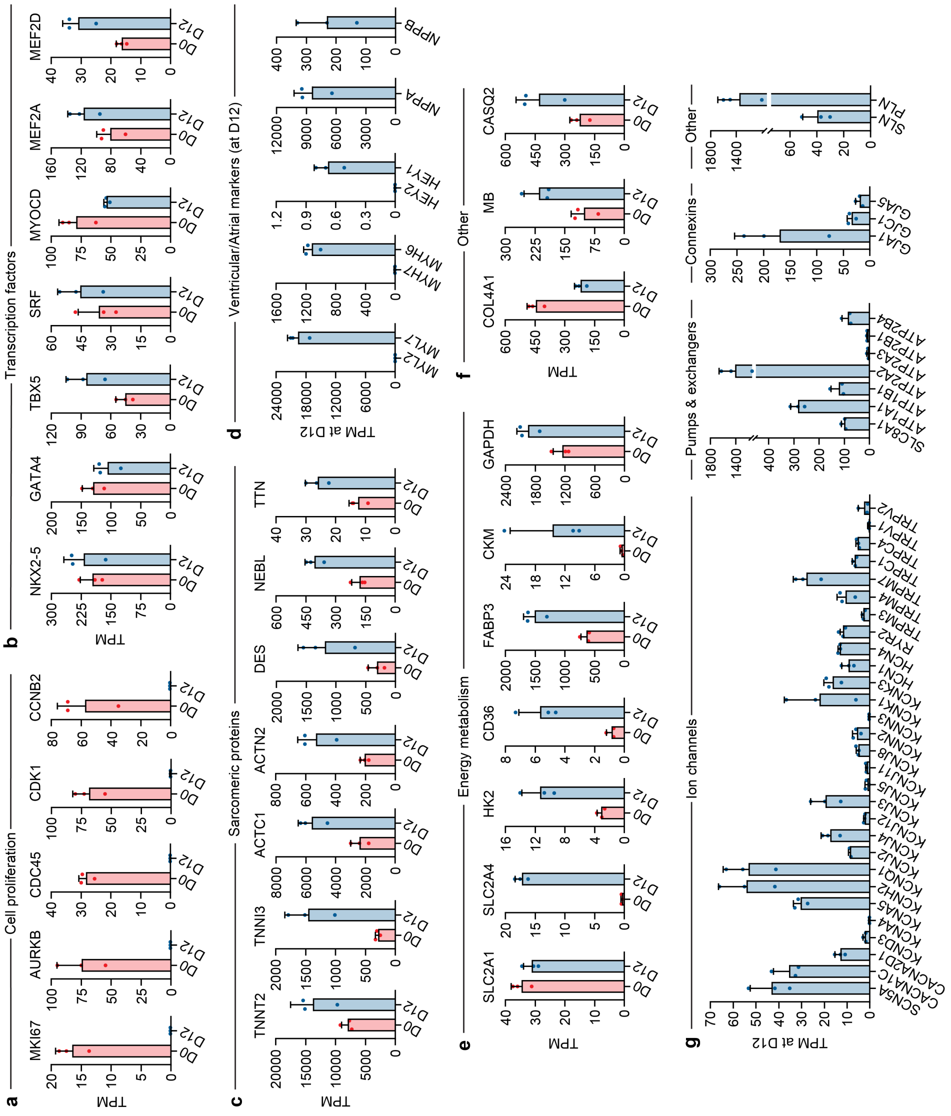

Supplemental Figure 7. Gene expression analysis by RNA-sequencing of hiAMs during proliferation (D0) and after differentiation (D12). Transcripts per million (TPM) are shown of genes **(a)** involved in cell proliferation, **(b)** encoding cardiac transcription factors, **(c)** coding for cardiac sarcomeric proteins, **(d)** preferentially expressed in atrial or ventricular cardiomyocytes, **(e)** involved in energy metabolism, and **(f)** encoding some other relevant genes. **(g)** TPM in differentiated hiAMs of genes involved in excitability, Ca^{2+} handling and electrical coupling. Bars represent mean gene expression levels in hiAM clones 2.38, 2.52 and 2.90 (*n* = 3 replicates per clone per time point). Error bars indicate SD. D0, zero days without dox. D12, twelve days without dox.

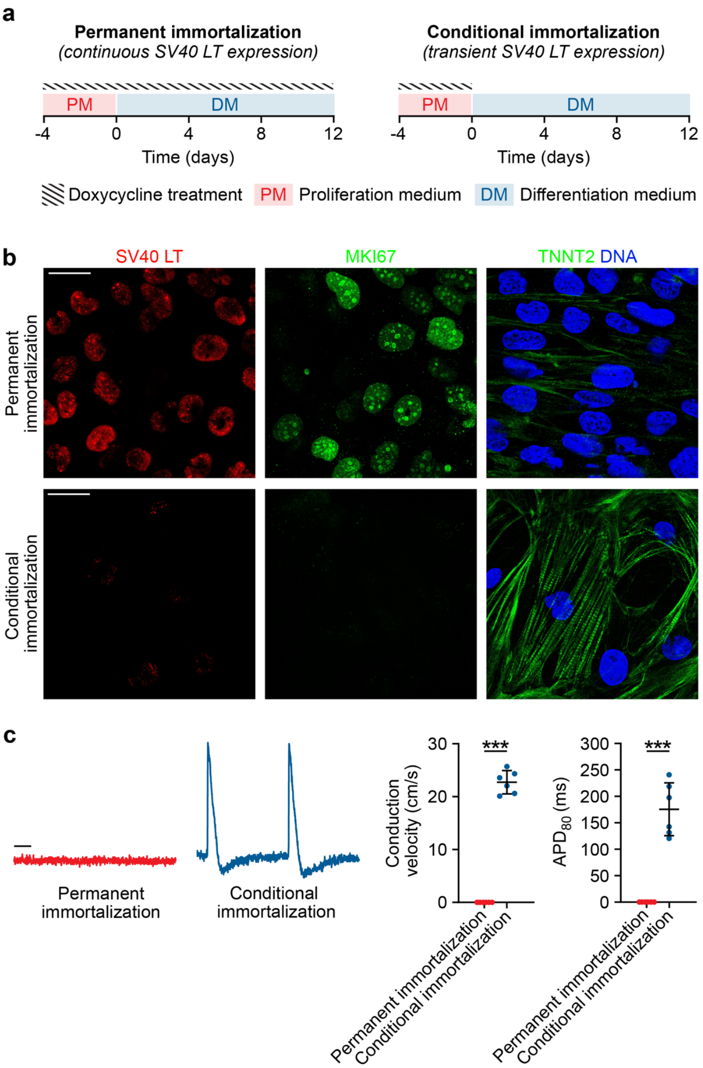

Supplemental Figure 8. Permanent cell immortalization vs. conditional cell immortalization. **(a)** Schematic overview of permanent immortalization (achieved through the continuous presence of dox) *vs.* conditional immortalization. In both cases, the proliferation medium was replaced by differentiation medium 12 days before analysis. **(b)** Immunofluorographs of hiAMs stained for Ki-67 (MKI67), SV40 LT and cardiac muscle troponin T (TNNT2) after 12 days of culture in differentiation medium. Scale bar, 25 µm. **(c)** Optical voltage mapping traces (left), CV and AP duration at 80% repolarization (APD_{80}) (right) after 12 days of culture in differentiation medium. Permanent LT expression precludes cardiomyogenic differentiation of hiAMs as evinced by the absence of excitable cells after 12 days of culture in differentiation medium. Scale bar, 200 ms. *n* = 6 layers from 2 independent differentiations. Mean shown, with error bars indicating SD. ***$P < 0.001$, unpaired *t*-test.

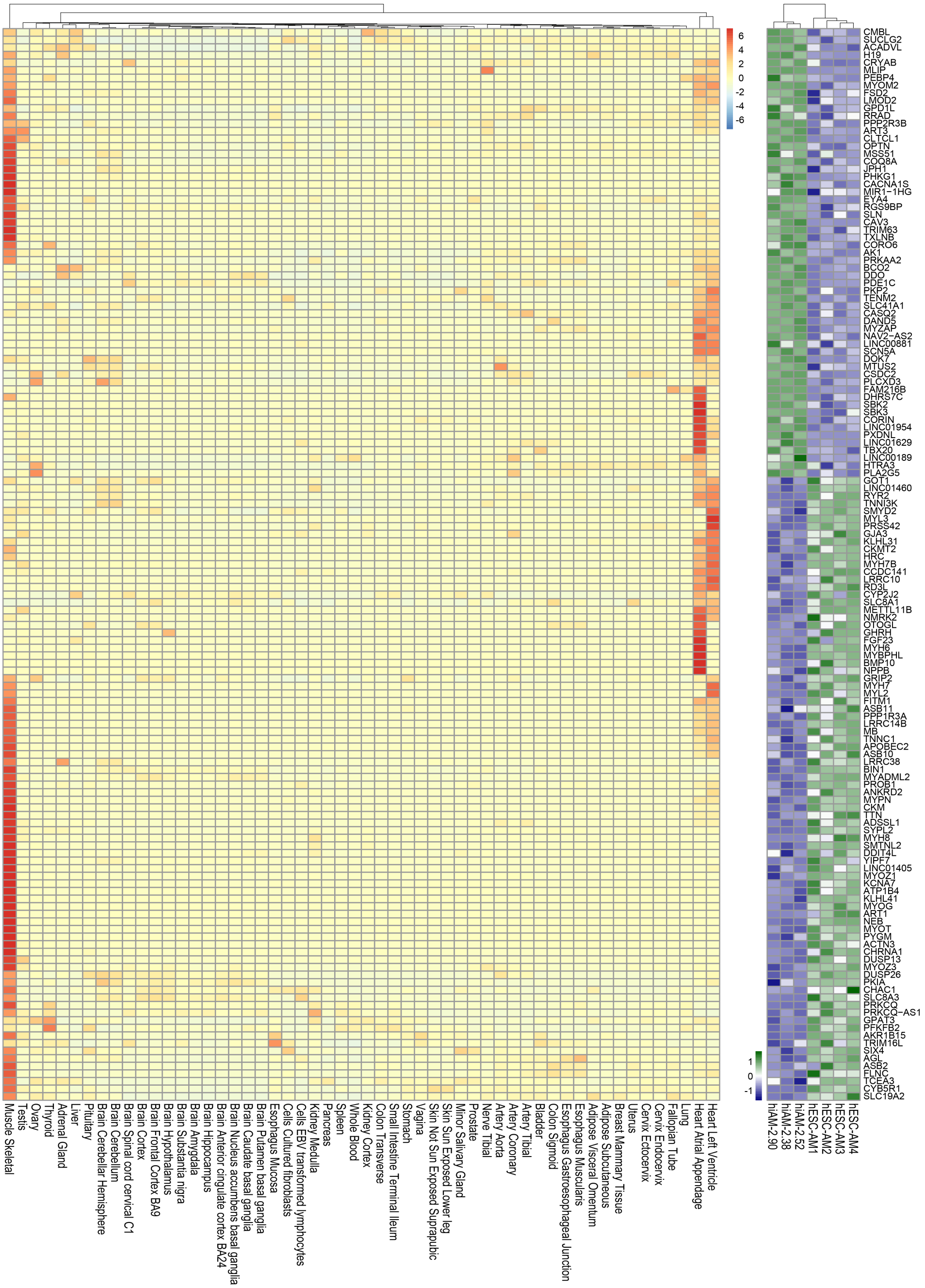

Supplemental Figure 9. Differential gene expression between hESC-AMs and hiAMs. Cluster of differentially expressed genes with striated muscle-specific expression. Expression levels shown in various human adult tissues (left) and in hiAMs and hESC-AMs (right). Scale bars indicate row-scaled and centred expression values. For better legibility of the figure (print version), visit doi.org/10.1038/s41551-021-00827-5

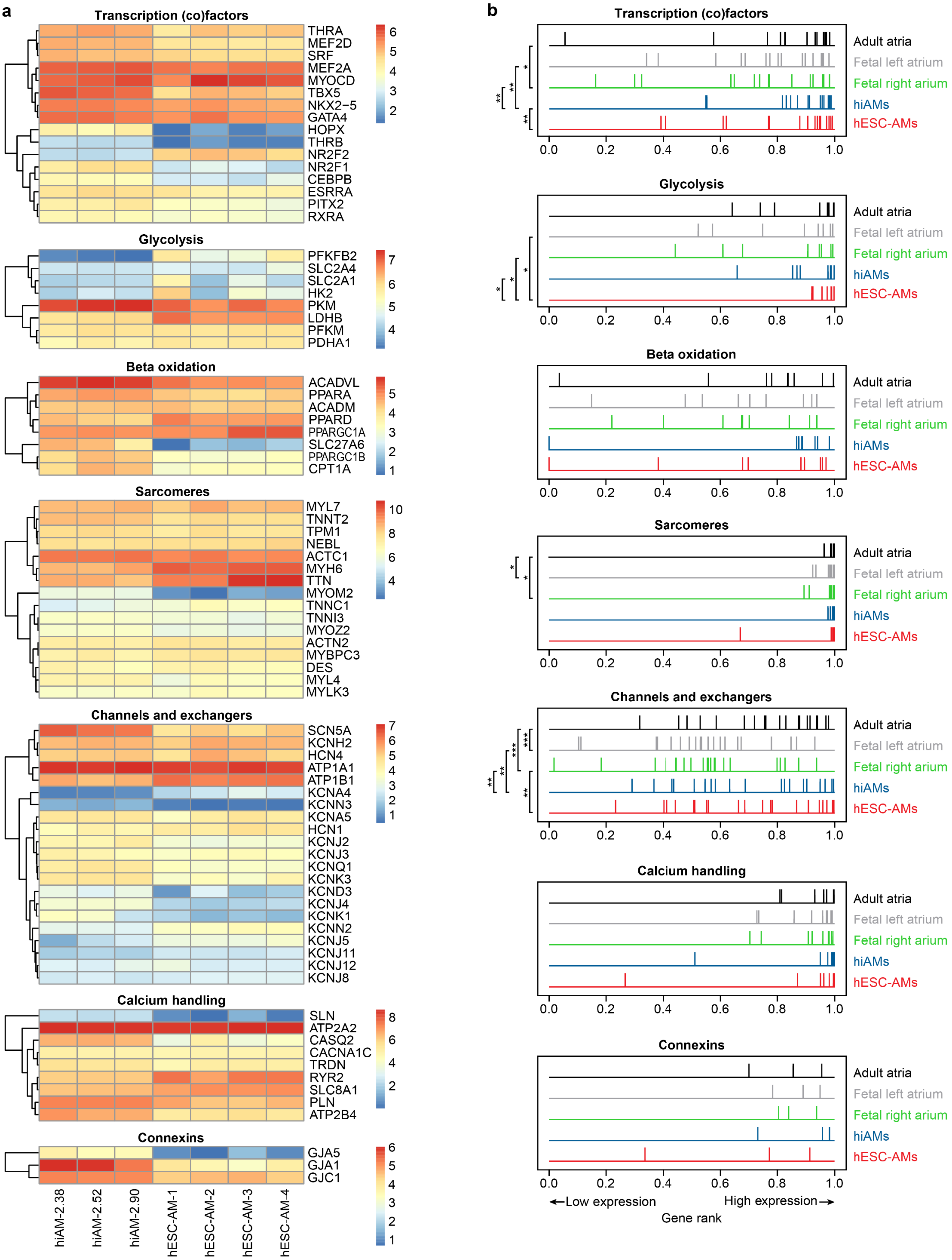

Supplemental Figure 10. Assessment of hiAM and hESC-AM maturity. **(a)** Expression of selected genes for comparison of the relative maturity of hiAMs and hESC-AMs. Scale bar indicates log-counts per million values. **(b)** Rank-based comparison of gene sets from **(a)** in human adult and foetal atria, differentiated hiAMs and hESC-AMs. *$P < 0.05$, **$P < 0.01$, ***$P < 0.001$, Wilcoxon signed-rank test.

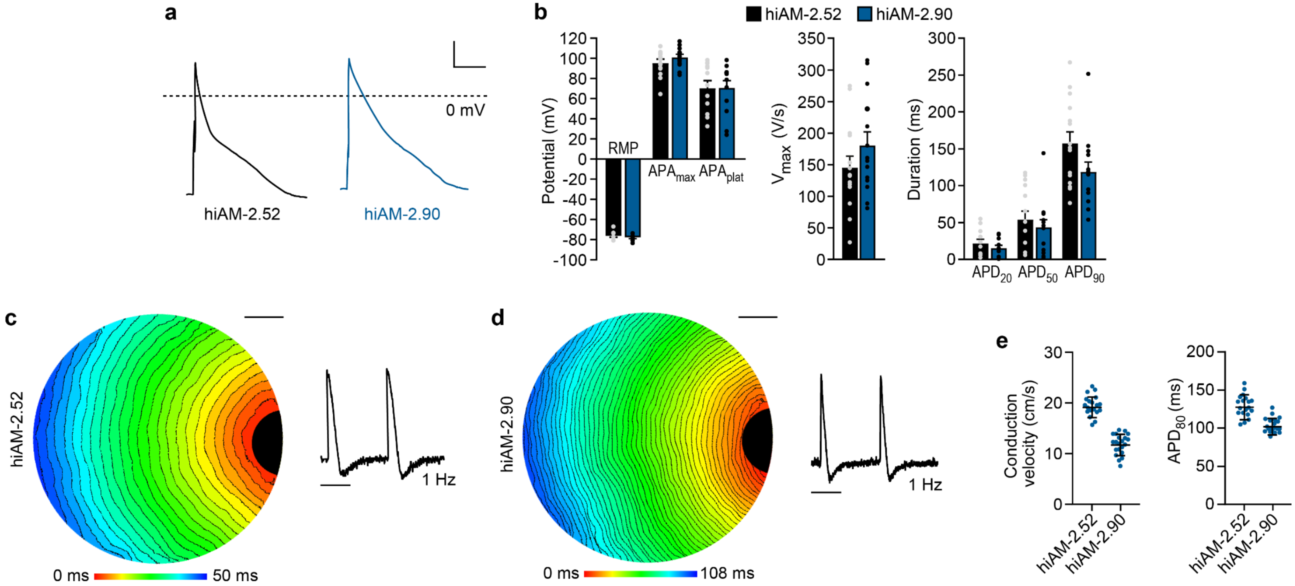

Supplemental Figure 11. Electrophysiological characterization of differentiated hiAM clones 2.52 and 2.90. **(a)** Representative AP traces and **(b)** mean AP parameters of single differentiated hiAM-2.52 (*n* = 13 cells from 3 independent differentiations) and single differentiated hiAM-2.90 (*n* = 14 cells from 3 independent differentiations) during 1-Hz electrical stimulation. Scale bars in **(a)** x = 50 ms, y = 20 mV. Dotted line in **(a)** indicates the zero mV level. RMP, resting membrane potential. APA$_{max}$, maximal AP amplitude. APA$_{plat}$, AP plateau amplitude. V$_{max}$, maximum AP upstroke velocity. APD$_{20/50/90}$, AP duration at 20, 50 and 90% of repolarization. Error bars indicate standard error of the mean (SEM). **(c, d)** Representative activation maps and optical voltage traces of differentiated **(c)** hiAM-2.52 and **(d)** hiAM-2.90 layers (24-well format). Isochrones, 2 ms. Scale bar of maps, 2 mm. Scale bar of traces, 500 ms. **(e)** Mean CV and APD$_{80}$ in confluent layers of differentiated hiAM-2.52 (*n* = 19 layers from 4 independent differentiations) and hiAM-2.90 (*n* = 21 layers from 3 independent differentiations). Mean shown, with error bars indicating SD.

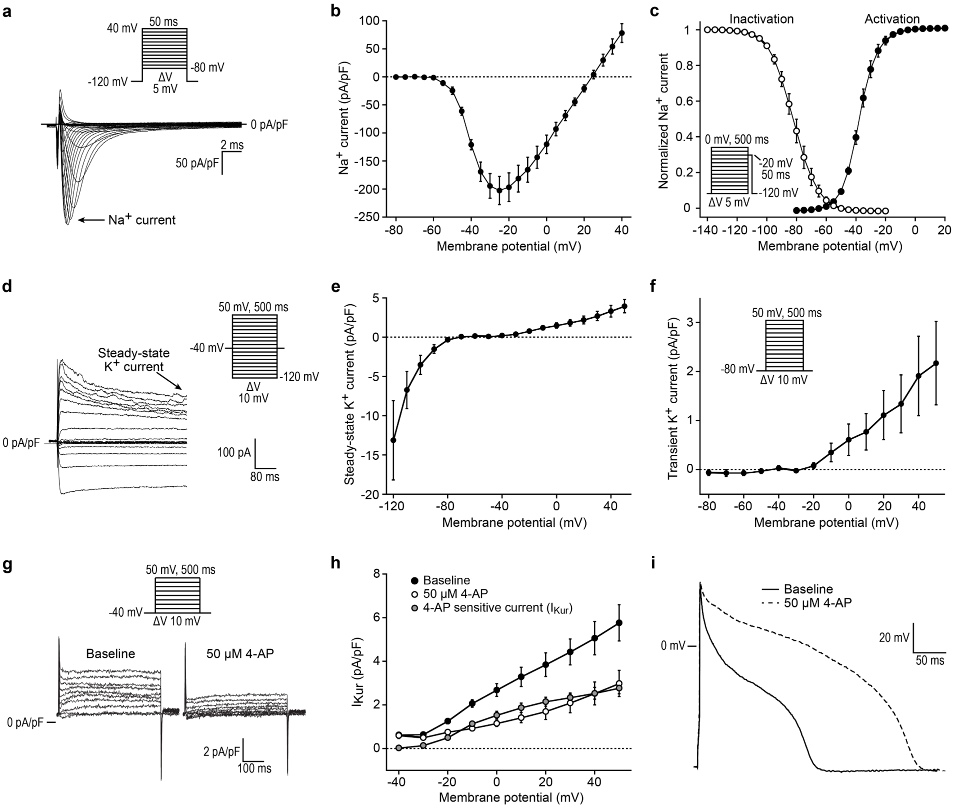

Supplemental Figure 12. Membrane currents in hiAM-2.38. **(a)** Voltage clamp protocol and typical examples of Na^+ currents. **(b)** Average current-voltage (I-V) relationship of the Na^+ current. **(c)** Voltage dependency of (in)activation. Inset, voltage clamp protocol used to measure voltage dependency of inactivation. $V_{1/2}$ was -37.1 ± 1.0 and -81.0 ± 1.8 mV for activation and inactivation, respectively. Slope factor k was 5.8 ± 0.6 and -5.9 ± 0.3 mV for activation and inactivation, respectively. **(b, c)** *n* = 9 cells from 3 independent differentiations. **(d)** Voltage clamp protocol and typical examples of steady-state K^+ currents. **(e)** Average I-V relationship of the steady-state current. *n* = 11 cells from 4 independent differentiations. **(f)** Average I-V relationship of the transient outward K^+ current. Inset, voltage clamp protocol used. *n* = 10 cells from 4 independent differentiations. **(g)** Voltage clamp protocol and typical examples of steady-state currents in absence and presence of 50 μM 4-aminopyridine (4-AP). **(h)** Average I-V relationship of the 4-AP-sensitive ultrarapid delayed rectifier K^+ current (I_{Kur}). *n* = 6 cells from 2 independent differentiations. **(i)** Typical example of the effects of I_{Kur} blockade on APs with 50 μM 4-AP. The average effects on APs are shown in Supplemental Table 4. **(b, c, e, f, h)** Mean shown, with error bars indicating SEM.

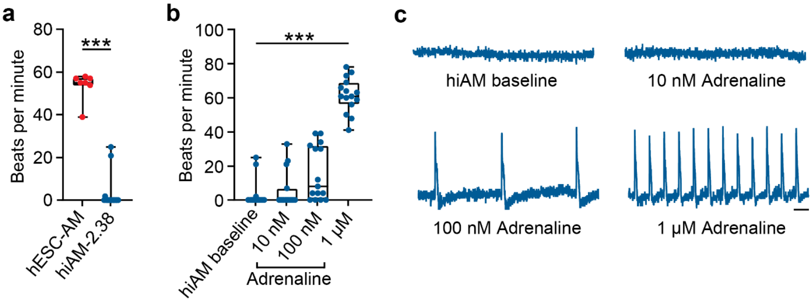

Supplemental Figure 13. Spontaneous activity of hESC-AM and hiAM layers. **(a)** Spontaneous beating rate of hESC-AM (red, *n* = 7 layers from 3 independent differentiations) and hiAM-2.38 (blue, *n* = 15 layers from 3 independent differentiations) layers. Beats per minutes defined as the number of APs measured by optical voltage or Ca^{2+} mapping per minute. ***$P < 0.001$, Mann-Whitney test. **(b)** Effect of an increasing concentration of adrenaline (Sigma-Aldrich, E4642) on the beating rate of hiAM-2.38 layers, revealing their chronotropic responsiveness to adrenoreceptor stimulation. *n* = 15 layers from 3 independent differentiations. ***$P < 0.001$, Friedman with Dunn *post-hoc* analysis comparing to baseline. **(a, b)** Median and quartiles are shown, error bars indicate minimum and maximum values. **(c)** Representative optical voltage traces of hiAM layers exposed to different adrenaline concentrations. Scale bar, 1 sec.

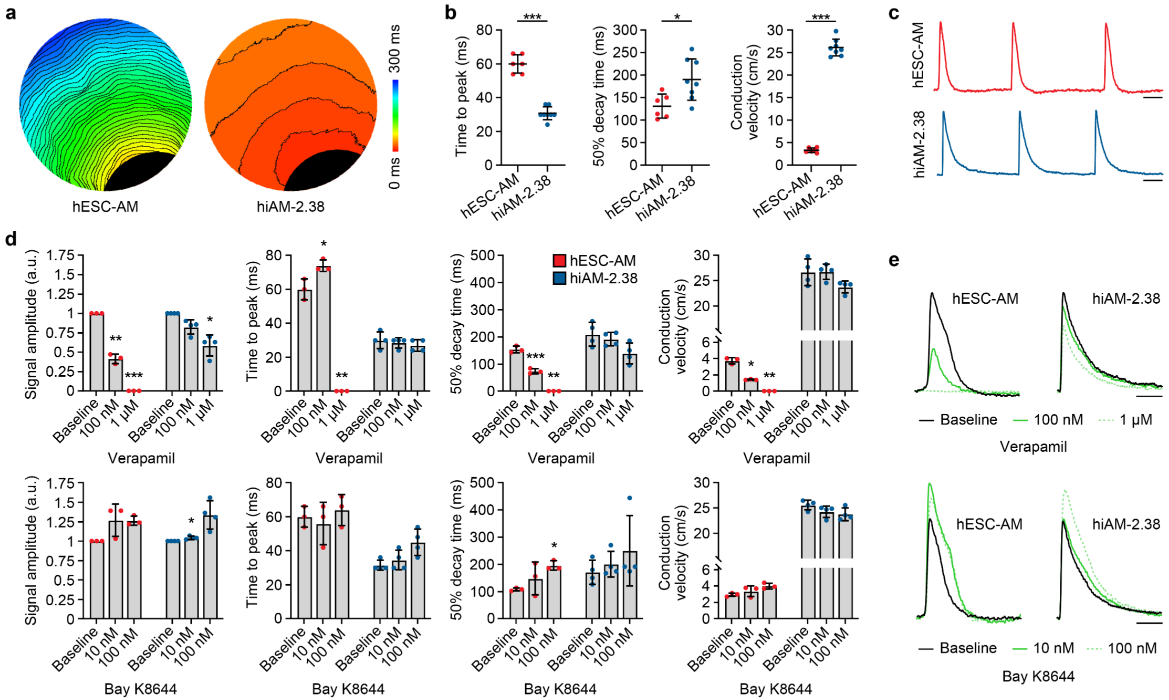

Supplemental Figure 14. Ca^{2+} transients of hESC-AMs and differentiated hiAMs. **(a)** Representative activation maps of hESC-AM and hiAM-2.38 layers (48-well format). Isochrones, 6 ms. **(b)** Mean time to peak, 50% decay time and CV of Ca^{2+} transients in hESC-AM (n = 6 layers from 2 independent differentiations) and hiAM-2.38 (n = 8 layers from 2 independent differentiations) layers. $P < 0.05$, ***$P < 0.001$, unpaired t-test. Mean shown, with error bars indicating SD. **(c)** Representative optical Ca^{2+} traces. Scale bar, 500 ms. **(d)** Effect of L-type Ca^{2+} channel antagonist (verapamil) or agonist (Bay K8644) addition on Ca^{2+} transients in hESC-AMs (n = 3 layers from 2 independent differentiations) and hiAMs (n = 4 layers from 2 independent differentiations). a.u., arbitrary units. *$P < 0.05$, **$P < 0.01$, ***$P < 0.001$, repeated measures analysis of variance with Dunnett *post-hoc* analysis compared to baseline. Mean shown, with error bars indicating SD. **(e)** Representative optical Ca^{2+} traces in the absence and presence of verapamil and Bay K8644. Scale bar, 250 ms.

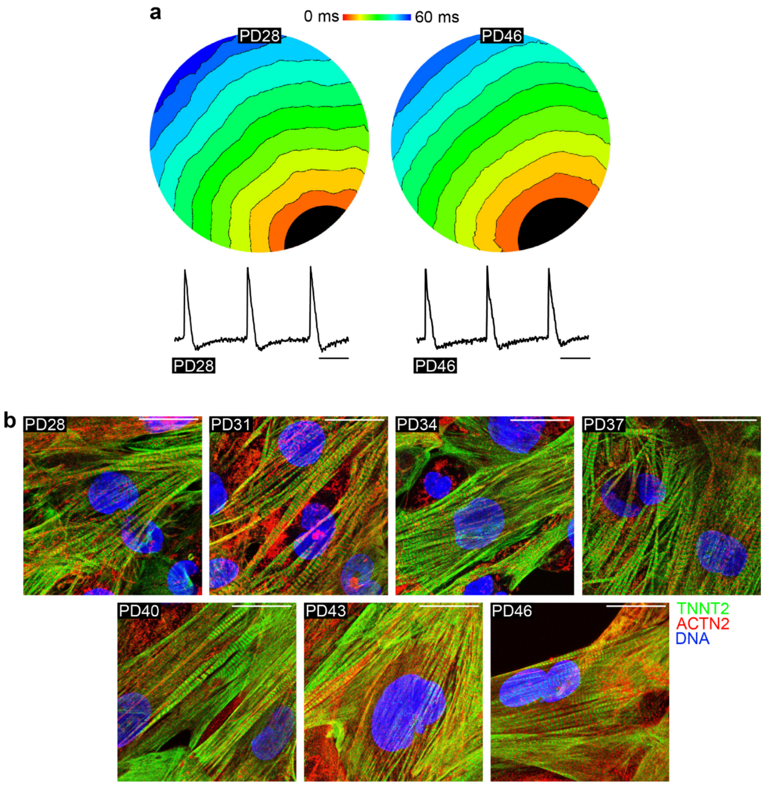

Supplemental Figure 15. Differentiation capacity of hiAMs at different PDs. **(a)** Representative activation map and optical voltage traces of differentiated hiAM-2.38 layer at PD 28 and at PD 46 (24-well format). Isochrones, 6 ms. Scale bar, 500 ms. **(b)** Immunostaining patterns of α-actinin 2 (ACTN2) and cardiac troponin T (TNNT2) of differentiated hiAMs at different PDs (from PD28 through PD46). Scale bar, 25 μm.

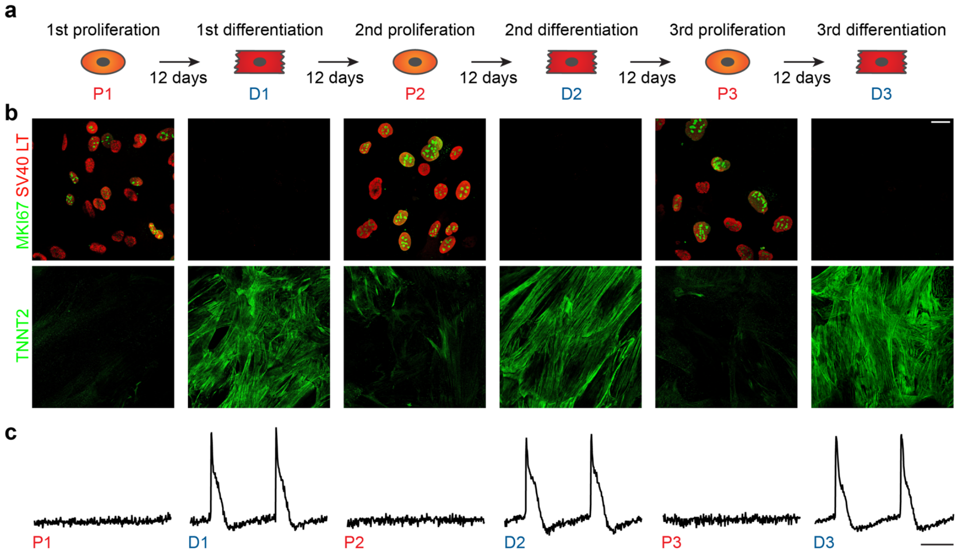

Supplemental Figure 16. Repeated switching of hiAMs between proliferation and differentiation. **(a)** Schematic overview of repeated switching of hiAM-2.38 between proliferation and differentiation. Each transition takes approximately 12 days. **(b)** Immunostaining patterns of SV40 LT, Ki-67 (MKI67) and cardiac muscle troponin T (TNNT2) showing full maintenance of cardiomyogenic differentiation ability during 3 successive cycles of hiAM-2.38 proliferation and differentiation. Scale bar, 25 µm. **(c)** Representative optical voltage traces of hiAM layers at the described time points, showing repeated loss and gain of excitability. Scale bar, 500 ms.

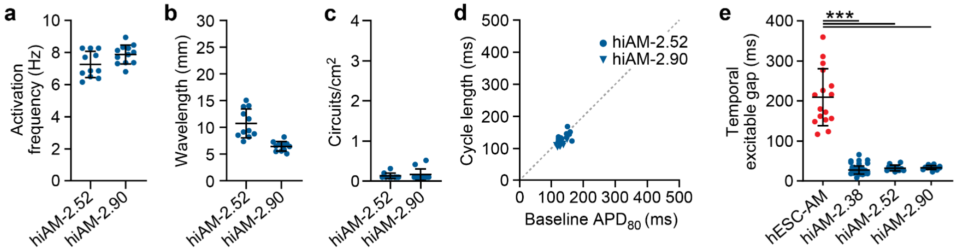

Supplemental Figure 17. Arrhythmia characteristics of differentiated hiAM-2.52 and -2.90 cultures. **(a)** Mean activation frequency, **(b)** wavelength and **(c)** arrhythmia complexity (*i.e.* the number of reentrant circuits per cm^2) of hiAM-2.52 and -2.90 cultures following induction of reentrant circuits. **(d)** Correlation between baseline APD$_{80}$ and cycle length of induced reentrant circuits in hiAM-2.52 and -2.90 cultures. **(e)** Temporal excitable gap in arrhythmic hESC-AM and hiAM-2.38, -2.52 and -2.90 cultures. hESC-AM: *n* = 7 independent cultures, hiAM-2.38: *n* = 56 independent cultures. ****P* < 0.001, one-way analysis of variance with Tukey *post-hoc* analysis. **(a-c, e)** Mean shown, with error bars indicating SD. **(a-e)** hiAM-2.52: *n* = 11 independent cultures, hiAM-2.90: *n* = 12 independent cultures.

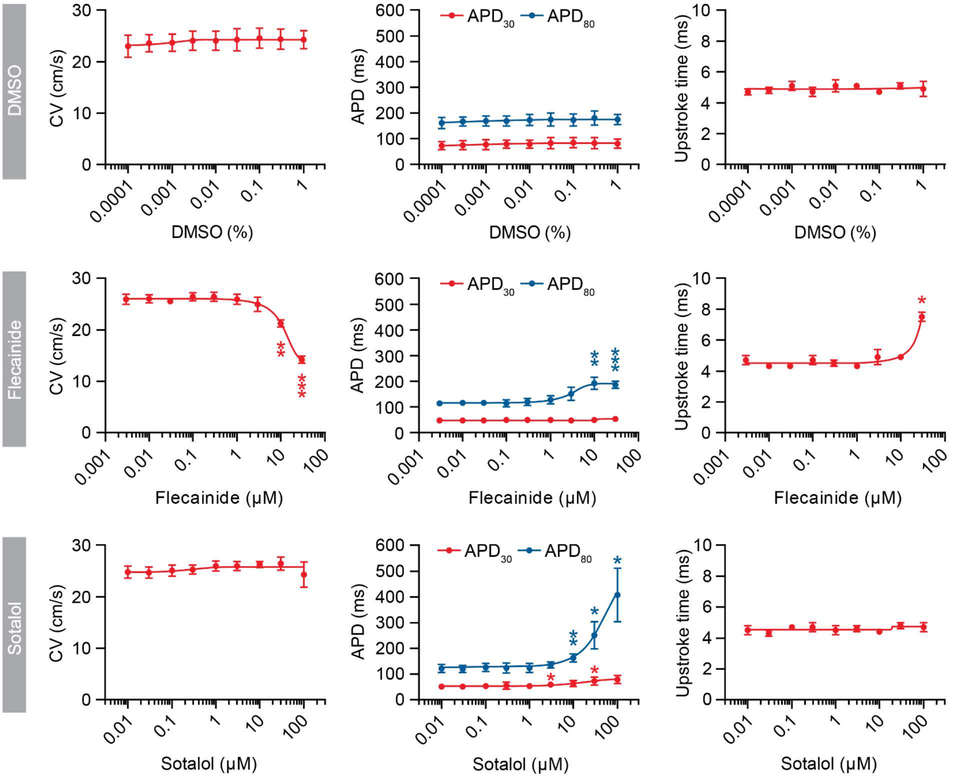

Supplemental Figure 18. Dose-dependent effects of flecainide and sotalol on differentiated hiAM cultures. Effects of DMSO (solvent/vehicle control), flecainide and sotalol at increasing concentrations on CV, AP duration at 30/80% repolarization ($APD_{30/80}$) and upstroke time in differentiated 2-cm^2 hiAM-2.38 cultures as measured by optical voltage mapping. Concentrations were increased until cultures were no longer excitable. *n* = 5 layers per compound for CV and APD, *n* = 3 layers for upstroke time. Mean shown, with error bars indicating SD. *$P < 0.05$, **$P < 0.01$, ***$P < 0.001$, repeated measures analysis of variance with Dunnett *post-hoc* analysis with the lowest concentrations serving as control (threshold $P < 0.01$ for *post-hoc* analyses).

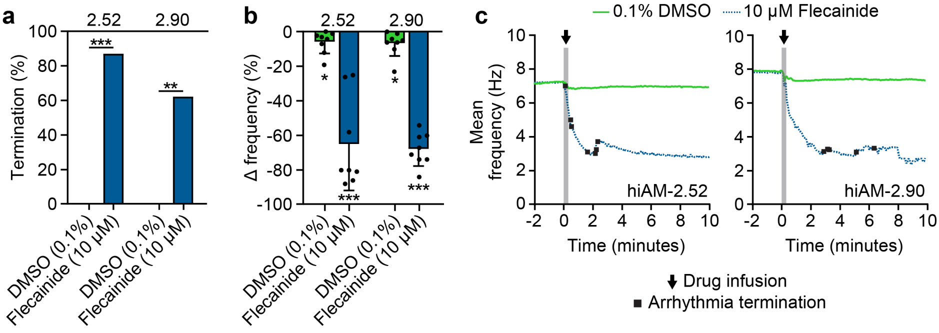

Supplemental Figure 19. Effects of flecainide on arrhythmic hiAM-2.52 and -2.90 cultures. **(a)** Rate of reentrant circuit termination and **(b)** change (Δ) in activation frequency in arrhythmic 10-cm^2 cultures of differentiated hiAM-2.52 and -2.90 at 10 min after infusion of 0.1% DMSO or 10 μM flecainide compared to baseline. Mean shown, with error bars indicating SD. **(c)** Continuous monitoring of mean activation frequency in arrhythmic hiAM- 2.52 and -2.90 cultures prior to and after infusion of 0.1% DMSO or 10 μM flecainide. **(a-c)** $n = 8$ for each compound and hiAM clone. $^*P<0.05$, $^{***}P < 0.001$. **(a)** Chi-square test. **(b)** Paired *t*-test.

Supplemental Figure 20 (next page). Arrhythmia dynamics and termination following antiarrhythmic drug infusion. **(a)** Pie chart showing the frequency of arrhythmia termination and of the 3 main mechanisms causing arrhythmia termination using combined data from hiAM-2.38, -2.52 and -2.90. **(b)** Arrhythmia parameters measured at various time points prior to and following antiarrhythmic drug infusion. Number of hiAM-2.38 cultures with arrhythmic activity present at 0, 0.5, 2, 5, 10 min: 0.1% DMSO (8, 8, 8, 8, 8), 30 μM sotalol (9, 8, 7, 7, 7) and 10 μM flecainide (8, 7, 7, 5, 2). Mean shown, shaded area indicates SD. **(c)** Visualization of the position of the arrhythmia core in time. Left, infusion of 0.1% DMSO not resulting in arrhythmia termination. Middle, 10 μM flecainide infusion resulting in drifting and subsequent collision of the core with the boundary, thereby terminating arrhythmic activity. Right, 10 μM flecainide infusion resulting in collision and termination of 2 cores with opposite chirality. Time between points is 18 ms.

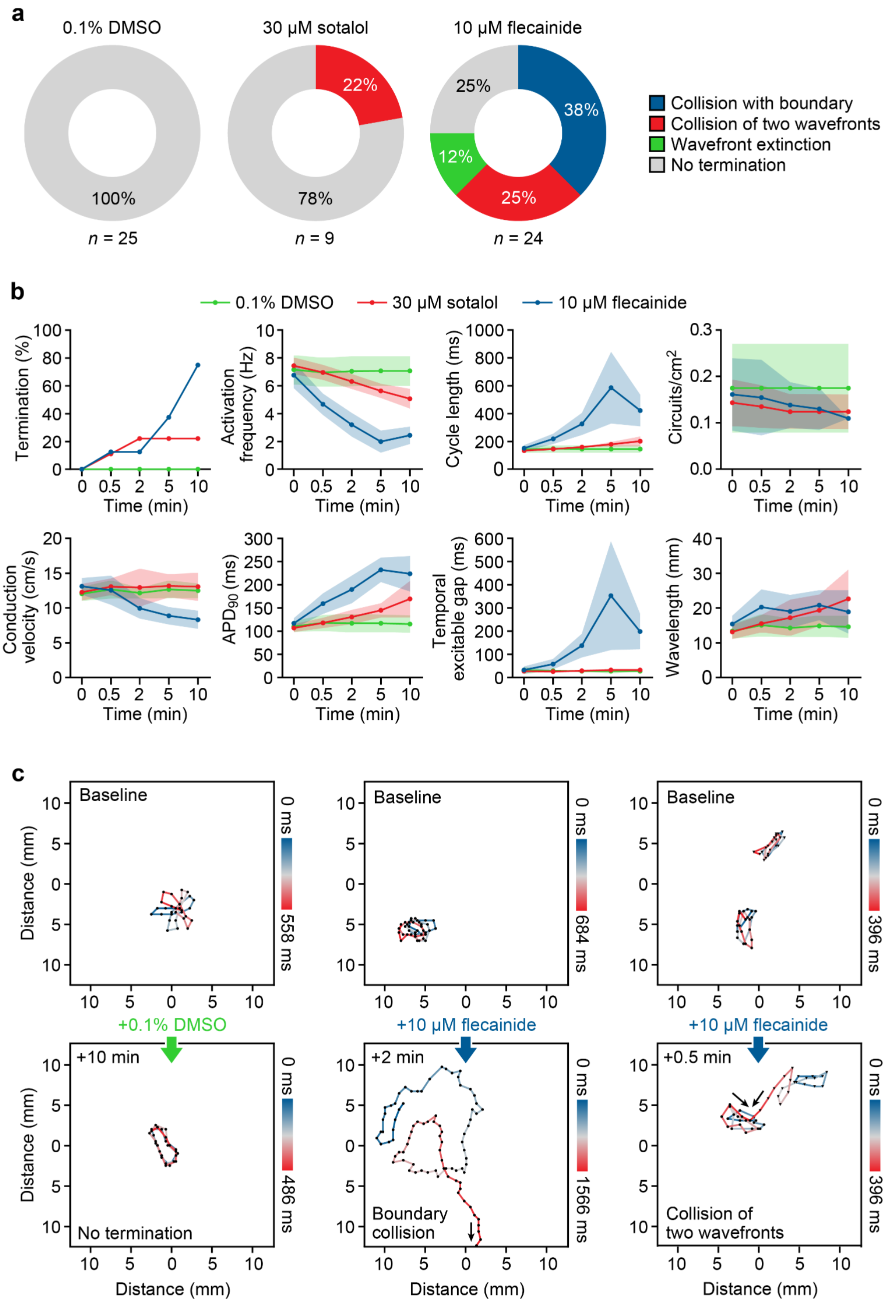

Supplemental Figure 20

(legend on previous page)

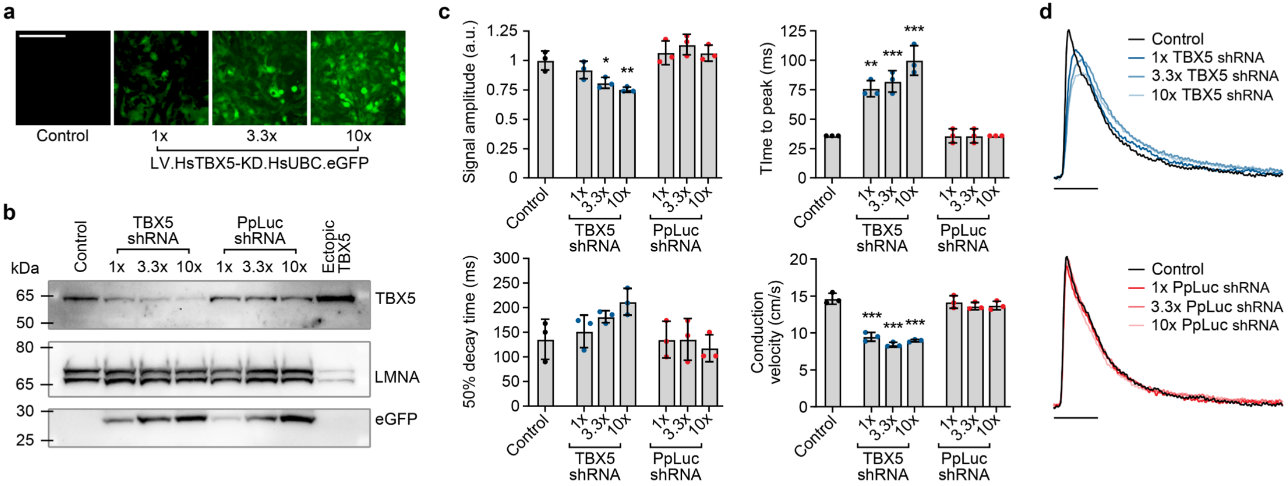

Supplemental Figure 21. Effect of TBX5 knockdown during hiAM differentiation on Ca^{2+} transients. **(a)** Immunofluorographs of differentiated hiAM-2.52 layers transduced with increased doses of the TBX5-specific shRNA-encoding LV. Scale bar, 200 µm. **(b)** TBX5 and eGFP levels in differentiated hiAMs expressing different amounts of TBX5-specific shRNAs and, as negative control, firefly luciferase (PpLuc)-specific shRNAs. LMNA is visualized as loading control. Ectopically expressed TBX5 is included as positive/size control. See **Supplemental File 4** for uncropped blots. **(c)** Ca^{2+} transient characteristics of differentiated hiAM layers ($n = 3$ per group) expressing different amounts of TBX5-specific and PpLuc-specific shRNAs. a.u., arbitrary units. Mean shown, with error bars indicating SD. $^{*}P < 0.05$, $^{**}P < 0.01$, $^{***}P < 0.001$, one-way analysis of variance with Dunnett *post-hoc* analysis comparing to the control condition. **(d)** Representative optical Ca^{2+} transients of hiAM layers in the different conditions. Scale bar, 250 ms.

Supplemental Table 1. Lentiviral integration sites.

Clone	Integration site	Region
hiAM-2.38	chr3_39,185,198	CSRNP1 - Exon
	chr8_67,467,802	Non-coding area
	chr8_67,467,886	Non-coding area
	chrX_15,297,016	Non-coding area
hiAM-2.52	chr3_155,019,560	Non-coding area
	chr3_155,019,563	Non-coding area
	chr5_151,196,079	Non-coding area
	chr8_56,615,904	Non-coding area
	chr8_71,038,196	NCOA2 - Intron
hiAM-2.90	chr1_46,308,658	MAST2 - Intron
	chr7_94,588,214	PPP1R9A - Intron
	chr8_54,909,384	TCEA1 - Intron
	chr17_1,081,463	ABR - Intron
	chr19_4,724,095	Non-coding area
	chr19_44,735,866	ZNF227 - Intron

Supplemental Table 2. Ploidy of differentiated hiAMs.

Clone	Near-diploid			Aneuploid 1			Aneuploid 2			
	%	DI	%CV	%	DI	%CV	%	DI	%CV	RCS
hiAM-2.38	5.2	0.9	5.3	77.7	1.7	4.4	17.1	3.3	4.0	2.9
hiAM-2.52	3.3	0.9	2.8	93.2	1.7	4.3	3.5	3.7	4.3	3.2
hiAM-2.90	12.0	0.9	5.3	81.4	1.8	5.3	6.6	3.4	4.2	3.2

%, percentage of total population. DI, DNA index. %CV, % coefficient of variation. RCS, reduced Chi-square of ModFit LT analysis.

Supplemental Table 3. AP parameters of hfAMs, hiAMs and haAMs.

Parameter	hfAM ($n = 6$)	hiAM-2.38 ($n = 39$)	hiAM-2.52 ($n = 13$)	hiAM-2.90 ($n = 14$)	haAM ($n = 9$)
RMP (mV)	-74.5 (1.0)	-81.4 (0.7)***	-76.5 (1.2)	-77.9 (0.9)*	-78.3 (2.2)
APA_{max} (mV)	85.2 (6.0)	109.1 (1.8)***	95.4 (3.7)	101.0 (2.6)**	120.2 (3.3)
APA_{plat} (mV)	47.0 (4.0)	72.8 (4.0)*	70.5 (7.2)*	71.2 (6.5)*	58.4 (3.7)
V_{max} (V/s)	130 (28)	220 (19)	148 (21)	181 (22)	333 (33)
APD_{20} (ms)	6 (2)	13 (2)	24 (6)*	16 (4)	5 (2)
APD_{50} (ms)	37 (15)	46 (6)	58 (13)	44 (10)	27 (11)
APD_{90} (ms)	152 (27)	153 (11)	162 (17)	119 (13)	216 (36)

haAM, human adult AM. RMP, resting membrane potential. APA_{max}, maximal AP amplitude. APA_{plat}, AP plateau amplitude. V_{max}, maximum AP upstroke velocity. $APD_{20/50/90}$, action potential duration at 20%, 50% and 90% of repolarisation. Data presented as mean (SEM). *$P < 0.05$, **$P < 0.01$, ***$P < 0.001$, unpaired t-test comparing hiAMs to hfAMs.

Supplemental Table 4. Average effects of I_{Kur} blockade on hiAM-2.38 action potentials.

Parameter	Baseline ($n = 6$)	50 µM 4-AP ($n = 6$)	*P*-value
RMP (mV)	-80.1 (1.5)	-80.6 (1.5)	0.82
APA_{max} (mV)	111.3 (5.3)	118.0 (2.0)	0.17
APA_{plat} (mV)	83.1 (4.2)	110.1 (1.8)	< 0.001
V_{max} (V/s)	279.8 (32.4)	281.2 (31.9)	0.78
APD_{20} (ms)	18 (8)	86 (13)	< 0.001
APD_{50} (ms)	86 (9)	223 (18)	0.001
APD_{90} (ms)	206 (9)	296 (27)	0.01

RMP, resting membrane potential. APA_{max}, maximal AP amplitude. APA_{plat}, AP plateau amplitude. V_{max}, maximum AP upstroke velocity. $APD_{20/50/90}$, action potential duration at 20%, 50% and 90% of repolarisation. Data presented as mean (SEM). Paired t-test.

Supplemental Table 5. Antibodies.

Antigen	Host	Dilution	Supplier	Catalogue# (number)
SV40 LT	Mouse	1:400 (ICC) 1:5,000 (WB)	Santa Cruz	sc-147
MKI67	Rabbit	1:400 (ICC)	Abcam	ab15580
ACTN2	Mouse	1:400 (ICC) 1:100 (FC)	Sigma-Aldrich	A7811
TNNT2	Rabbit	1:400 (ICC) 1:100 (FC)	Abcam	ab45932
MYL7	Rabbit	1:400 (ICC)	Abcam	ab127001
MYL2	Mouse	1:50 (ICC)	Enzo	ALX-BC-1150-S-L001
GJA1	Rabbit	1:400 (ICC)	Sigma-Aldrich	C6219
NKX-2.5	Mouse	1:400 (ICC)	Santa Cruz	sc-376565
GAPDH	Mouse	1:10,000 (WB)	Merck	MAB374
TBX5	Goat	1:400 (WB)	Santa Cruz	sc-17866
GJA5	Goat	1:400 (WB)	Santa Cruz	sc-20466
eGFP	Rabbit	1:12,500 (WB)	Thermo Fisher	A11122
LMNA	Rabbit	1:5,000 (WB)	Santa Cruz	sc-20681

Antigen	Host	Dilution	Supplier	Catalogue#	Conjugate
Rabbit IgG (H+L)	Goat	1:50,000 (WB)	Abcam	ab97080	HRP
Goat IgG (H+L)	Donkey	1:5,000 (WB)	Santa Cruz	sc-2020	HRP
Mouse IgG (H+L)	Goat	1:10,000 (WB)	Abcam	ab97040	HRP
Mouse IgG (H+L)	Donkey	1:400 (ICC)	Thermo Fisher	A10037	Alexa Fluor 568
Rabbit IgG (H+L)	Donkey	1:400 (ICC) 1:200 (FC)	Thermo Fisher	A21206	Alexa Fluor 488
Mouse IgG (H+L)	Donkey	1:200 (FC)	Thermo Fisher	A21202	Alexa Fluor 488

ICC, immunocytochemistry. FC, flow cytometry. WB, western blot. HRP, horseradish peroxidase.

Supplemental Table 6. Primer pairs used for shRNA cloning.

Construct	Forward primer	Reverse primer
TBX5 shRNA	ccgg**GATACAAATTCGCAGATAATA**ctcgagTATTATCTGCGAATTTGTATCtttttg	aattcaaaaa**GATACAAATTCGCAGATAATA**ctcgagTATTATCTGCGAATTTGTATC
Ppluc shRNA	ccgg**CGCTGAGTACTTCGAAATGTC**ctcgagGACATTTCGAAGTACTCAGCGtttttg	aattcaaaaaC**GCTGAGTACTTCGAAATGTC**ctcgagGACATTTCGAAGTACTCAGCG

Sense (bold) and antisense sequences of the targeted genes are shown in capital letters.

Supplemental Video 1. Contractions of hfAMs and hiAMs. Spontaneous contractions in hfAM and hiAM-2.38 cultures. Scale bar, 1 mm. Video available at: doi.org/10.1038/s41551-021-00827-5

Supplemental Video 2. Optical voltage mapping of hESC-AM and hiAM layers. Optical voltage mapping recordings during 1-Hz electrical stimulation (white dots represent pacing electrode and electrical stimulation). Playback at 1/6 of real time speed. Scale bar, 2 mm. Video available at: doi.org/10.1038/s41551-021-00827-5

Supplemental Video 3. Induction of reentrant activity in hESC-AM and hiAM layers. Induction of reentrant activity through high frequency stimulation in hESC-AM and hiAM-2.38 layers (white dots represent pacing electrode and electrical stimulation). Playback at 1/3 of real time speed. Scale bar, 5 mm. Video available at: doi.org/10.1038/s41551-021-00827-5

Supplemental Video 4. hiAM arrhythmic activity with varying degrees of complexity. Three examples of atrial arrhythmias of different complexities as determined by the number of reentrant circuits present in the hiAM-2.38 layers following induction. Playback at 1/3 of real time speed. Scale bar, 1 cm. Video available at: doi.org/10.1038/s41551-021-00827-5

Supplemental Video 5. Effects of antiarrhythmic drugs on reentrant activity in hiAM layers. Effect of 0.1% DMSO, 30 μM sotalol and 10 μM flecainide on reentrant activity in hiAM layers after infusion. DMSO infusion has no effect on arrhythmic activity, whereas 30 μM sotalol reduces the activation frequency by 34% after 10 minutes. Flecainide (10 μM) infusion results in termination of arrhythmic activity, after which 1-Hz electrical stimulation results in normal conduction. Playback at 1/3 of real time speed. Scale bar, 5 mm. Video available at: doi.org/10.1038/s41551-021-00827-5

Supplemental Data File 1. Differentially expressed genes hiAM D0 vs D12. Data file available at: doi.org/10.1038/s41551-021-00827-5

Supplemental Data File 2. Differentially expressed genes hiAM vs hESC-AM. Data file available at: doi.org/10.1038/s41551-021-00827-5

Supplemental Data File 3. Individual (raw) data points and *P*-values. Data file available at: doi.org/10.1038/s41551-021-00827-5

Supplemental Data File 4: Uncropped western blots. Data file available at: doi.org/10.1038/s41551-021-00827-5